KINETICS OF FIELD EVAPORATION

A STUDY OF MOLECULES IN HIGH ELECTRIC FIELDS

by

Brenden Scott Nickerson

Submitted in partial fulfilment
of the requirements for the degree of

Master of Science

at

Dalhousie University

Halifax, Nova Scotia
August 2015

To my family

Table of Contents

List of Figures . . . . . **v**

Abstract . . . . . **viii**

List of Abbreviations and Symbols . . . . . **ix**

Acknowledgements . . . . . **xi**

1 Introduction **1**

2 A ground state understanding **5**

2.1 Background theory: Hartree equations and beyond 5

2.1.1 The Hartree equations 6

2.1.2 The Hartree-Fock equations 7

2.1.3 Beyond Hartree-Fock equations 7

2.1.4 Basis sets 9

2.1.5 Geometry optimization 10

2.2 Field evaporation of polymers 10

2.2.1 Perfluoro-decanethiolate in an applied electric field 11

2.2.2 Amino-undecanethiolate in an applied electric field 16

2.2.3 Comparison with Experiment 17

2.3 Summary 18

3 Kinetics of field evaporation **19**

3.1 Theoretical construction 21

3.1.1 Adiabatic states 22

3.1.2 Diabatic states 24

3.1.3 Two state system 27

3.1.4 Kinetics 28

3.1.5 The master equation 29

3.2 Implementation 31

3.2.1 The ground state adiabatic potential energy V_0 31

3.2.2 The potential energy of a neutral species W_{00} 32

3.2.3 The potential energy of ionic species W_{nn}, $n > 0$ 34
3.2.4 Diabatic transition potential energy W_{01}, transformation angle θ, first excited adiabatic state V_1 36
3.2.5 Wave function normalization 37
3.2.6 Width of bound state levels and occupation 41
3.3 Field evaporation of polymers 43
3.4 Summary 48

4 Conclusion **50**

Bibliography **52**

List of Figures

1.1 Simplified cartoon of the atom probe setup. Edge atoms, highlighted in red, are the first to field evaporate from the probe tip with initiation coming from a pulsed laser. 1

1.2 Lines of constant potential in the region of a conducting surface with hemispherical boss at zero potential. Axis values are in units of hemisphere radius a, and lines of constant potential are -0.1, -0.2, -0.3, -0.4, -0.5 in units of $\tilde{E}_0 a$ where $\Phi = -z\left(1 - 1/(x^2+z^2)^{3/2}\right)$. 3

2.1 Zero field structures for (A) helical perfluoro-decanethiolate and (B) all-trans amino-undecanethiolate adsorbed on Cu. Colouring of atoms, F= light blue, C= grey, H= white, S= yellow, Cu= red, N= dark blue. 11

2.2 Evaporated species from perfluoro-decanethiolate. Applied electric field values are quoted for the model using a single copper base (Cu) and a three copper base (Cu_3). 12

2.3 Effect of applying a field to a tilted polymer. The polymer here is perfluoro-decanethiolate adsorbed to a three copper base (Cu_3). 13

2.4 Electrostriction experienced by perfluoro-decanethiolate. Length is between terminal carbon and the copper base atom. 14

2.5 Solid circle: dipole moment $\boldsymbol{p}$ [eÅ] along the field axis (+z) of perfluoro-decanethiolate. Dashed triangle: electric polarizability α [eÅ^2/V]. Dotted square: dielectric constant ε. 15

2.6 HOMO/LUMO gap of perfluoro-decanethiolate in an applied electric field until evaporation. 15

2.7 Solid circle: dipole moment $\boldsymbol{p}$ [eÅ] along the field axis (+z) of amino-undecanethiolate. Dashed triangle: electric polarizability α [eÅ^2/V]. Dotted square: dielectric constant ε. 16

2.8 Evaporated species from amino-undecanethiolate. Applied electric field values are quoted for the model using a single copper base (Cu) and a three copper base (Cu_3). 17

3.1 Coulomb style potential with applied homogeneous electric field for an atom of radius r_0 showing the electron tunnelling out of the atom from the highest occupied level E_H. 19

3.2 Adiabatic potential energy curves, V_0, for the field evaporation of the terminal CF_3 group leaving the remaining perfluoro-decanethiolate polymer adsorbed on Cu, applied fields of (0.0, 0.8, 1.0, 1.2) V/Å. 31
3.3 Diabatic potential energy functions W_{00} and W_{11} found through fitting the adiabatic curve V_0 of Figure 3.2 at 0.8 V/Å. 32
3.4 Morse fit to the region $\{0 \leq z \leq z_0 \,|\, E \leq 0\}$ of the potential energy curve for the field evaporation of the terminal CF_3 group leaving the remaining perfluoro-decanethiolate polymer adsorbed on Cu, applied fields of (0.0, 0.8, 1.0, 1.2) V/Å. Note the curve for 0.8 V/Å lay nearly atop that of 0.0 V/Å. 33
3.5 Bound state wave functions of W_{00}, fit to the region $\{0 \leq z \leq z_0 \,|\, E \leq 0\}$ of V_0, for the field evaporation of the terminal CF_3 group leaving the remaining perfluoro-decanethiolate polymer adsorbed on Cu at 0.8 V/Å. The insert shows the wave functions for the first five levels. The adiabatic potential energy V_0 is shown as a dashed line, and W_{00} as dash-dot line. 34
3.6 Continuum wave function with energy -2.5 eV of the potential energy W_{11}, fit to the asymptotic slope of V_0, for a singly charged CF_3 group leaving the remaining perfluoro-decanethiolate polymer adsorbed on Cu with an applied field of 0.8 V/Å. The adiabatic potential energy V_0 is shown as a dashed line, and W_{11} as dash-dot line. 35
3.7 Linear fit for both W_{11} where $F_1 = e\tilde{E}$, and W_{22} given by the asymptotic slope. 36
3.8 Diabatic transition potential energy W_{10} for the field evaporation of terminal CF_3 group leaving the remaining perfluoro-decanethiolate polymer adsorbed on Cu with an applied field of 0.8 V/Å. V_0 shown as dashed line. 37
3.9 Wave functions of a triangular potential energy well given by Airy functions. β_i are the locations of the zeros of the Airy function which define the allowed states. As the width of the well L gets larger, the allowed energy levels sink to lower energies while becoming more closely spaced. 38
3.10 Airy function representing the wave function of a particle in homogeneous external field. β_i are the locations of the zeros. The units of amplitude $[A]$ depend on normalization. 38
3.11 Left: Density of states (left), $g(E)$; Right: integrated density of states, $G(E)$, for discrete bound states. Each level contributes a delta function to the density of states, where the spacing between allowed levels becomes smaller as energy increases. 42
3.12 Lorentzian profile for the extent of a bound state energy level. This is the density of states as a function of energy. 42
3.13 Left: Density of states, $g(E)$; Right: integrated density of states, $G(E) = \int_{-\infty}^{E} dE' g(E')$, for the bound states of CF_3 at 0.8 V/Å, where each level contributes a Lorentzian with a width of 1 eV. 43

3.14 Left: W_{00} in the region of the minimum for the field evaporation of the terminal CF_3 group leaving the remaining perfluoro-decanethiolate polymer adsorbed on Cu, applied fields of (0.0, 0.2, 0.4, 0.6, 0.8) V/Å. Right: The minimum of W_{00} as a function of applied field. 44
3.15 Right: Transition rate $t_{10}(\mu, 0)$ from the ground state of W_{00} to a final energy state μ of W_{11} for the field evaporation of the terminal CF_3 from perfluoro-decanethiolate on Cu at 0.8 V/Å. The maximum transition rate from the ground state is to a final energy state in W_{11} of -1.82 eV. Left: Wave functions and potentials involved in this transition rate from the ground state. 45
3.16 Left: Surface map for the transition rate $t_{10}(\mu, \nu)$ for the field evaporation of the terminal CF_3 group leaving the remaining perfluoro-decanethiolate polymer adsorbed on Cu at 0.8 V/Å. The maximum transition rate for each bound level ν of W_{00} is highlighted by the overlaid red line. Right: The maximum transition rate $t_{10}(\mu, \nu)$ for each bound level ν of W_{00}. 46
3.17 Ion yield for the field evaporation of the terminal CF_3 group leaving the remaining perfluoro-decanethiolate polymer adsorbed on Cu_3 enforcing $F = q\tilde{E},\ q = 1.0e$. 47
3.18 Ion yield for the field evaporation of the terminal $CF_3/C_2F_5/C_3F_7$ groups leaving the remaining perfluoro-decanethiolate polymer adsorbed on Cu_3 enforcing $F = q\tilde{E},\ q = 1.0e$ at 0.8 (left) and 1.0V/Å (right). 48

Abstract

Field Evaporation, the physical phenomenon harnessed in the atom probe microscope, describes the breaking apart of molecules in an electric field. Interest has shifted away from the well understood field evaporation of metals and towards a variety of semiconducting and insulating materials for which less is known. One such material commanding current interest is that of polymer self assembled monolayers due to their ability to provide coatings to arbitrary materials giving them novel chemical properties. Stoffers, Oberdorfer and Schmitz in [1] studied experimentally the field evaporation of both amino-undecanethiol and perfluoro-decanethiol SAMs which are the focus of this theoretical investigation.

Density functional theory is used to study the process of field evaporation itself along with trends such as electrostriction, charge transfer, polarizability and HOMO/LUMO gap leading up to the point of evaporation. Applying this theory to structures in electric fields on the order of volts per angstrom has given results that form the cornerstone of our theoretical understanding and investigation in this area.

For further understanding, a complementary kinetic theory of field evaporation [2] first developed for metals is also implemented which provides both time and temperature dependence. A better understanding of the ion yield is reached with the comparison between possible field evaporated species.

List of Abbreviations and Symbols Used

APT	atom probe tomography
DFT	density functional theory
HOMO	highest occupied molecular orbital
LUMO	lowest unoccupied molecular orbital
SAM	self-assembled monolayer
TDDFT	time dependent density functional theory
A	unitary transformation matrix
$\hat{a}_{i\nu}$	annihilation operator of diabatic states
$\hat{a}_{i\nu}^{\dagger}$	creation operator of diabatic states
$\hat{b}_J$	annihilation operator of a phonon mode J
$\hat{b}_J^{\dagger}$	creation operator of a phonon mode J
e	charge of electron
E	energy
$\tilde{E}$	electric field
E_0	ground state energy
$E_{corr.}$	correlation energy
$E_{xc}[\rho]$	exchange-correlation energy
F	force
$g(E)$	density of states
$G(E)$	integrated density of states
$\hat{H}$	total Hamiltonian
$\hat{H}'$	interaction Hamiltonian
$\hat{H}_a$	adparticle Hamiltonian
$\hat{H}_e$	electronic Hamiltonian
$\hat{H}_T$	thermal Hamiltonian
$J[\rho]$	classical potential energy of electrons
n^{ph}	Boes-Einstein occupation function for phonons
$\boldsymbol{p}$	dipole moment
q	charge
$\boldsymbol{r}$	electron position
$\boldsymbol{R}$	nuclear position
$R(\mu, \nu)$	phonon transition rate
t_{flight}	time of flight
$T(\mu, \nu)$	transition rate
$T_s[\rho]$	classical kinetic energy of electrons

$\hat{T}_{el}$	electron kinetic energy operator
$\hat{T}_{ion}$	ion kinetic energy operator
$\boldsymbol{u}_J$	normal phonon mode
v_{eff}	effective potential energy for electrons
v_{xc}	exchange-correlation potential energy
V_0	adiabatic potential energy curve
V_1	adiabatic potential energy curve of first electronically excited state
$\hat{V}_{ion-ion}$	ion-ion potential energy operator
$\hat{V}_{ion-el}$	ion-electron potential energy operator
$\hat{V}_{el-el}$	electron-electron potential energy operator
W	diabatic interaction matrix
W_{00}	diabatic potential energy curve of a neutral species
W_{11}	diabatic potential energy curve of a singly charged species
W_{10}	diabatic transition potential energy
Y	ion yield
α	electric polarizability
β_i	i^{th} zero of the Airy function
Γ	width of bound state level
ε	dielectric constant
ε_0	Hartree-Fock energy
$\zeta_i(\boldsymbol{r};\boldsymbol{R})$	adiabatic many electron wave function
$\eta_{i\nu}(\boldsymbol{R})$	diabatic wave functions of adparticle nucleus
$\eta^0_{i\nu}(\boldsymbol{R})$	uncoupled diabatic wave functions of adparticle nucleus
$\xi_i(\boldsymbol{r};\boldsymbol{R})$	diabatic many electron wave functions
$\rho(\boldsymbol{r})$	electron density
τ_{BL}	Buttiker-Landauer time
Φ	electric potential
Φ	Airy function
$\chi_{i\alpha}(\boldsymbol{R})$	adiabatic wave function of adparticle nucleus
$\Psi_\alpha(\boldsymbol{r};\boldsymbol{R})$	eigenfunction of $\hat{H}_a$
Ψ	eigenfunction of $\hat{H}$
ω_J	frequency of normal phonon mode

Acknowledgements

Firstly, I would like to thank my supervisor Dr. H. J. Kreuzer who has been a mentor and inspirational figure in my education in physics, granting me many opportunities during my studies at Dalhousie University. His support has led me to conferences across Canada and in Germany which provided exposure to physics that could not be had at Dalhousie.

Thank you to my group members Markus Karahka, Patrick Shea, Elena Silaeva and Yu Xia. Especially to Markus for his guidance throughout my studies here at Dalhousie and his discussion and experience which aided my transition into the area of field evaporation.

Lastly, my family has been an immeasurable force that has propelled me to this point both in my education and life, it is to them that this work is dedicated.

1. Introduction

Field evaporation, the physical phenomenon harnessed in the atom probe microscope, describes the breaking apart of molecules and solids in an electric field. The atom probe, composed of a metallic tip on the order of 100 nm apex diameter and position-sensitive detector, evaporates the surface atoms of the tip by applying a constant voltage in the region of kilovolts between the tip and detector. This voltage difference creates an electrostatic field on the order of volts per angstrom in the direction of the detector. Electrons in the tip are displaced by the applied field exposing positively charged ions. If the field is strong enough the positive ions are pulled from the surface and accelerated towards the detector where they are recorded, Figure 1.1.

To gain a more accurate understanding of the rate of this process, field evaporation can be initiated by pulsing the tip with a femtosecond laser. This provides a kick either as a thermal or electronic excitation to the already polarized surface atoms and serves as a precise starting point for a time of flight measurement. Using this pulsing technique, both the position and the time of flight of the ions are known.

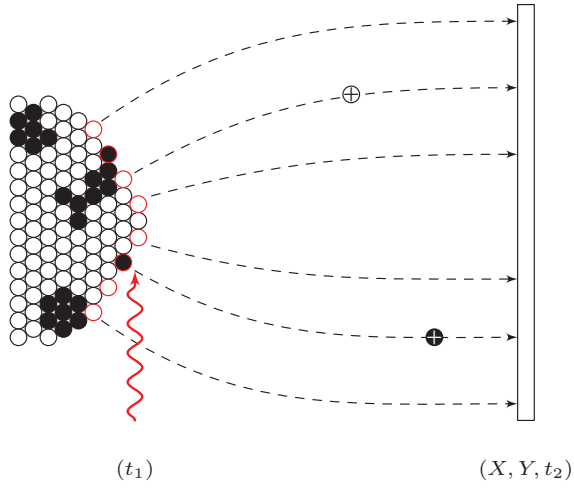

Figure 1.1: Simplified cartoon of the atom probe setup. Edge atoms, highlighted in red, are the first to field evaporate from the probe tip with initiation coming from a pulsed laser.

From the recorded data and knowledge of the field evaporation process a three dimensional layer-by-layer reconstruction of the tip with atomic resolution is possible. Common, reconstruction techniques rely on a projection model where by the field-evaporated ions recorded at a position (X, Y) on the detector are projected back along modelled electric field lines to a layer in the sample corresponding to the order of detection [3]. Along side the reconstruction of the sample, the time of flight measurements allow for a generation of a mass spectrum

for the field evaporated ions. At the point of ionization the evaporated ion has zero kinetic energy, it then increases due to acceleration by the electric field. The change in kinetic energy $T = mv^2/2$ is equal to the change in potential energy $V = ne\Phi$ giving the mass to charge ratio as

$$\frac{m}{n} = 2e\Phi \left(\frac{t_{flight}}{L} \right)^2 \tag{1.0.1}$$

where m is the mass of the ion, ne the ion charge, Φ the applied voltage difference and L the distance between source and detector. The time of flight is given by $t_{flight} = t_2 - t_1$ where t_1 is the time ionization occurs, corresponding to the laser pulse, and t_2 is the time of ion detection. Plotting the intensity or ion count versus mass to charge ratio allows for an analysis of the dominant field evaporated species. Spatial reconstruction and modelling of the imaging process is still a strong focus in current research [4–7] and is further developed through theoretical research of field evaporation.

The atom probe was first developed for use with metallic tips and as such a generalized theory for their evaporation based on quantum mechanics soon followed [8–13]. These results can be understood from a simple classical model posed in the popular book by Jackson [14], the scenario:

> *A large parallel plate capacitor is made up of two plane conducting sheets with separation D, one of which has a small hemispherical boss of radius a on its inner surface $D >> a$. The conductor with the boss is kept at zero potential, and the other conductor is at a potential such that far from the boss the electric field between the plates is $\tilde{E}_0$.*

Solving for the potential in the region of a conducting surface with a hemispherical protrusion was shown to represent a lone atom adsorbed to a conducting surface in an applied electric field well [11]. The solution

$$\Phi = -\tilde{E}_0 \left(r - \frac{a^3}{r^2} \right) \cos\theta. \tag{1.0.2}$$

is plotted in Figure 1.2 where $\tilde{E}_0 a$ is a unit of potential and a a unit of length, i.e $\Phi \to \Phi/\tilde{E}_0 a$ and $r \to r/a$ giving $\Phi = -z\left(1 - 1/r^3\right)$.

Solving for the electric field, $\tilde{E} = -\nabla\Phi$, in the region of the hemisphere gives

$$\tilde{E}_r = -\left.\frac{\partial\Phi}{\partial r}\right|_{r=a} = 3\tilde{E}_0 \cos\theta \tag{1.0.3}$$

where the field at the top of the hemisphere, $\tilde{E}_r = 3\tilde{E}_0$, is larger than the static field, $\tilde{E}_0$, far from the boss. The force, given by $F = q\tilde{E}$, is directed away from the surface for positive charges and is largest in this field enhanced region. Hence, exposed atoms protruding from a conducting material create a local field enhancement leading to their preferential evaporation.

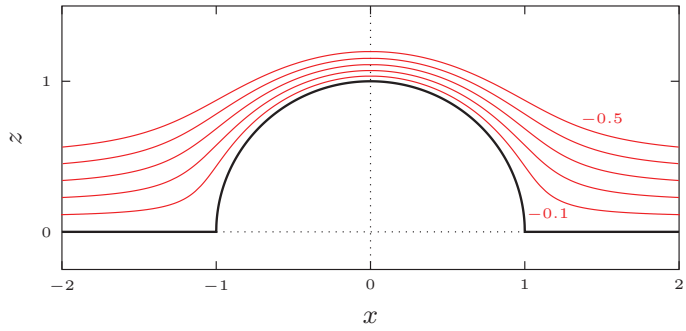

Figure 1.2: Lines of constant potential in the region of a conducting surface with hemispherical boss at zero potential. Axis values are in units of hemisphere radius a, and lines of constant potential are -0.1, -0.2, -0.3, -0.4, -0.5 in units of $\tilde{E}_0 a$ where $\Phi = -z\left(1 - 1/(x^2+z^2)^{3/2}\right)$.

Due to this field enhancement caused by the shielding of the electric field, field evaporation of metals occurs in an orderly fashion atom-by-atom evolving from edges, kink sites and protrusions from the conducting surface.

Interest has since shifted to the analysis of semiconductors and insulators. However, a strong theoretical understanding of their evaporation is in general still lacking. Although the phenomenon of field enhancement still plays an important role, the applied electric fields can penetrate insulating materials affecting the complete structure. This results in evaporation of not only single ions but clusters or molecules from the surface, whose composition depend on the field strength. As such the interpretation of the recorded data is difficult leading to poorer reconstructions of non-metallic samples.

Research continues in the areas of oxides, such as the experimental study of MgO both as a bulk structure and as inclusions in Fe using laser assisted atom probe tomography (APT) [15]. Theoretical studies [16, 17] were conducted to follow up on this work which confirmed the possible evaporated species successfully using density functional methods. Also more recent work has been done on ZnO [18, 19] and the phenomenon of metallization [20].

Self-assembled monolayers (SAMs) of polymer molecules have attracted much attention due to their ability to alter the surface properties of bulk materials. This feature allows for modification of existing structures as well as construction of surfaces with novel chemical properties. Areas of application include nanotechnology and organic electronics such as transistors.

Analysis of SAMs with the atom probe is still a new concept and comes with its own difficulties. Before recording data with the atom probe several layers are evaporated from the tip to remove any surface contamination. Unlike bulk structures or thick oxide layers studied previously in atom probe experiments, SAMs exist as a single layer on the surface of the emission tip making them more vulnerable to this cleaning process if employed. Furthermore, SAMs can be made of a variety of polymers composed of several different elements with vastly

different evaporation fields. This makes their analysis increasingly difficult as compared to simple crystalline structures containing one to three elements.

Few experimental studies of SAMs using the atom probe have been completed. Nishikawa and Taniguchi [21] used the scanning atom probe to analyze polythiophene by field evaporation. The dominant fragments as well as further analysis of the HOMO/LUMO gap and charge transfer was correctly determined using density functional methods by Wang, Kreuzer and Nishikawa [22]. Gault et al. [23] reported reconstruction of decanethiol SAMs; but some geometrical assumptions had to be made. Zhang and Hillier [24] considered evaporation of hexanethiolate SAMs for which they identified the dominant evaporated species showing a clear distinction between the SAM and the adsorbing gold surface. Stoffers, Oberdorfer and Schmitz [1] experimentally studied the evaporation of both amino-undecanethiol and perfluoro-decanethiol SAMs. The evaporated species in the case of perfluoro-decanethiol were identified as well as their evaporation field strength. Still the authors noted that the "present understanding of evaporation ... must be decisively improved before a spatial reconstruction of the evaporated volume becomes possible."

The objective of the following work is to develop a theoretical understanding of the evaporation of such SAMs. Two methods will be employed. Firstly, ground state density functional calculations will be used to find the evaporation field strength for the given structures as well as to study changes in physical properties with increasing field strength. To gain an understanding past the static, zero-Kelvin, ground-state calculations provided by density functional theory, a second method, first developed to look at the field evaporation of metals [2], will be used to consider the kinetics and temperature effects of field evaporation.

2. A ground state understanding

Density functional theory (DFT) is an inclusive term given to a set of methods used to calculate the ground state properties of materials. The premise is to consider the electron density $\rho(\boldsymbol{r})$ of the system and not the many-body Schrödinger equation. For a given system of N electrons the many-body wave function Ψ would depend on $3N$ spatial variables. However, the electron density will only ever depend on 3 spatial variables thus making its implementation faster than directly solving the Schrödinger equation.

DFT relies on the two Hohenberg-Kohn theorems which take advantage of the variational principle[1]. They state [27, p.51]: (1) the electron density $\rho(\boldsymbol{r})$ determines the number of electrons N and the external potential hence the ground-state wave function Ψ_0 and all other ground state properties of the system; (2) there exists a variational principle that states for a trial density $\tilde{\rho}(\boldsymbol{r})$, such that $\tilde{\rho}(\boldsymbol{r}) \geq 0$ and $\int d\boldsymbol{r}\, \tilde{\rho}(\boldsymbol{r}) = N$,

$$E_0 \leq E[\tilde{\rho}]$$

where E_0 is the ground state energy and $E[\tilde{\rho}]$ is the energy functional of trial electron density $\tilde{\rho}$. Levy [28] first showed that the variational principle could be written in terms of functionals of electron density, see also [27, p.56-60] for further explanation and other references of relevant works.

2.1 Background theory: Hartree equations and beyond

The problem of finding the ground state electronic structure of a system is simplified by the Born-Oppenheimer approximation also known as the adiabatic approximation [29, p.7]. This allows us to separate the total Hamiltonian into nuclear and electronic components by assuming their independence. Physically this is interpreted as a system of electrons moving in the potential created by fixed atomic nuclei. This defines the electronic Hamiltonian as

$$\hat{H}_e = \hat{T}_{el} + \hat{V}_{ion-ion} + \hat{V}_{ion-el} + \hat{V}_{el-el} \tag{2.1.1}$$

where T_{el} is the kinetic energy of the electrons and $V_{ion-ion}$, V_{ion-el}, and V_{el-el} are the interaction potential energies between the ions (nuclei-nuclei), ion-electron and electron-electron

[1] The variational principle of quantum mechanics can be used to guess the ground state energy of a system based on a guess of the wave function [25, §20] [26, p.33ff.]. Given a normalized wave function Ψ such that $\int dq\, \Psi^* \Psi = 0$ then,

$$\int dq\, \Psi^* \hat{H} \Psi \geq E_0$$

where E_0 is the ground state energy. The ground state is not degenerate thus the equality only holds for $\Psi = \Psi_0$ the ground state wave function.

respectively[2]. $V_{ion-ion}$ is a constant for a fixed arrangement of nuclei and is thus usually ignored. Here the only difference between $\hat{H}$ and $\hat{H}_{el}$ is the omission of the kinetic energy of the atomic nuclei.

2.1.1 The Hartree equations

A common starting point in the explanation of DFT methods are the Hartree equations which can be found in every book on the topic including popular books by Parr and Yang or by Ashcroft and Mermin[27, 30].

To solve a quantum mechanical problem involving many particles the many-body Schrödinger equation must be solved. The Hartree equations assume (1) that all particles (electrons) are independent or non-interacting other than through an averaged coulomb style potential. Therefore we can write the total wave function as a product of single electron wave functions

$$\Psi(r_1, \ldots, r_N) = \psi(r_1) \ldots \psi(r_N) \tag{2.1.2}$$

(2) ions are heavy and as such look fixed from the point of view of the electrons, hence, the kinetic energy of the ions is ignored and the ion-ion potential is said to be constant thus also ignored (Born-Oppenheimer). This simplifies the problem to a set of one electron Schrödinger equations called the Hartree equations

$$\left(-\frac{\hbar^2}{2m}\nabla^2 + V_{ion-el} + V_{el-el} \right) \psi_i(r) = \varepsilon_i \psi_i(r). \tag{2.1.3}$$

[2]In a simplistic sense we can write classical forms

$$\begin{aligned}
\hat{T}_{ion} &= -\frac{\hbar^2}{2}\sum_I \frac{\nabla_I^2}{M_I} \\
\hat{T}_{el} &= -\frac{\hbar^2}{2m}\sum_i \nabla_i^2 \\
\hat{V}_{ion-ion} &= -\frac{1}{8\pi\varepsilon_0}\sum_{I\neq J} \frac{Z_I Z_J}{|\boldsymbol{R}_I - \boldsymbol{R}_J|} \\
\hat{V}_{ion-el} &= -\frac{1}{4\pi\varepsilon_0}\sum_{i,I} \frac{Z_I e}{|\boldsymbol{r}_i - \boldsymbol{R}_I|} \\
\hat{V}_{el-el} &= \frac{1}{8\pi\varepsilon_0}\sum_{i\neq j} \frac{e^2}{|\boldsymbol{r}_i - \boldsymbol{r}_j|} \\
&= = -e\int d\boldsymbol{r}'\rho(\boldsymbol{r}')\frac{1}{|\boldsymbol{r} - \boldsymbol{r}'|} \\
\rho_i(\boldsymbol{r}) &= -e|\psi_i(\boldsymbol{r})|^2
\end{aligned}$$

However, this ignores the quantum phenomena of exchange and correlation. They are implicitly part of the Hamiltonian, but the exact functional form is not known. Hence the equalities above are approximations that must be supplemented.

2.1.2 The Hartree-Fock equations

Classically the motions of electrons are not correlated. However in reality electrons, having half-integer spin, are fermions and as such must obey Pauli's principle: in a system consisting of identical fermions, no two or more particles can be in the same state at the same time. Consequently, the motions are correlated in quantum mechanics.

Schrödinger's equation and hence the Hamiltonian do not account for the spin of particles because the spin does not affect their electrical interaction. We know however from Pauli's principle that electrons cannot occupy the same energy level unless their spins are antiparallel. Therefore the possible energy values of the system of electrons depends on their total spin. This is bizarrely reflected in the energy values given by Schrödinger's equation even though it does not directly consider the spin [25, p.227-233].

Pauli's principle requires that the electronic wave function be anti-symmetric upon exchange of any two electrons, i.e,

$$\Psi(r_1, \ldots, r_i, \ldots, r_j, \ldots, r_N) = -\Psi(r_1, \ldots, r_j, \ldots, r_i, \ldots, r_N). \tag{2.1.4}$$

This phenomenon is not satisfied by the independent electron approximation of the Hartree equations (2.1.2). The simplest wave function that will satisfy Pauli's principle can be written in the form of a Slater determinant of one electron wave functions,

$$\Psi(r_1 s_1, \ldots, r_N s_N) = \begin{vmatrix} \psi_1(r_1 s_1) & \psi_1(r_2 s_2) & \ldots & \psi_1(r_N s_N) \\ \psi_2(r_1 s_1) & \psi_2(r_2 s_2) & \ldots & \psi_2(r_N s_N) \\ \vdots & \vdots & & \vdots \\ \psi_N(r_1 s_1) & \psi_N(r_2 s_2) & \ldots & \psi_N(r_N s_N) \end{vmatrix} \tag{2.1.5}$$

From the variational principle $\varepsilon_0 \equiv \langle \Psi | \hat{H} | \Psi \rangle \equiv \frac{(\Psi, \hat{H}\Psi)}{(\Psi, \Psi)} \geq E_0$ the expectation value of the Hamiltonian will always be larger or equal to the true ground state energy. Using this wave function, and the original Hamiltonian a similar set of one electron Schrödinger equations can be found, called the Hartree-Fock equations,

$$\left(-\frac{\hbar^2}{2m}\nabla^2 + V_{ion-el} + V_{el-el} \right) \psi_i(r) - \sum_j \int d\boldsymbol{r'} \frac{e^2}{|\boldsymbol{r} - \boldsymbol{r'}|} \psi_j^*(\boldsymbol{r'}) \psi_i(\boldsymbol{r'}) \psi_j(\boldsymbol{r}) \delta_{s_i s_j} = \varepsilon_i \psi_i(r). \tag{2.1.6}$$

The last term is the result of exchange which is simply the correlation of parallel spin electrons given by Pauli's principle.

2.1.3 Beyond Hartree-Fock equations

The exact wave function can usually not be expressed as a single Slater determinant, therefore the resultant energy from Hartree-Fock, ε_0 is larger than the exact amount, E_0. The difference is termed the correlation energy $E_{corr.} = \varepsilon_0 - E_0$. This energy is the result of the correlation

between electrons that is not considered in Hartree-Fock, such as correlation between electrons of opposite spin.

Kohn-Sham equations

Kohn and Sham [31] developed the so-called Kohn-Sham (KS) equations as a method to solve the system of interacting fermions in a potential. This was done by the construct of an effective potential that acts on a system of non-interacting particles which generates the same density as the interacting system. The KS equations are listed here[3]

$$T_s[\rho] = \sum_{i=1}^{N} \sum_{s} \psi_i^*(\boldsymbol{r}) \left(\frac{1}{2} \nabla^2 \right) \psi_i(\boldsymbol{r}) \tag{2.1.9}$$

$$\begin{aligned} v_{eff}(\boldsymbol{r}) &= v(\boldsymbol{r}) + \frac{\delta J[\rho]}{\delta \rho(\boldsymbol{r})} + \frac{\delta E_{xc}[\rho]}{\delta \rho(\boldsymbol{r})} \\ &= v(\boldsymbol{r}) + \int d\boldsymbol{r}' \frac{\rho(\boldsymbol{r}')}{|\boldsymbol{r} - \boldsymbol{r}'|} + v_{xc}(\boldsymbol{r}) \end{aligned} \tag{2.1.10}$$

$$v_{xc}(\boldsymbol{r}) = \frac{\delta E_{xc}[\rho]}{\delta \rho(\boldsymbol{r})} \tag{2.1.11}$$

$$\left[-\frac{1}{2} \nabla^2 + v_{eff}(\boldsymbol{r}) \right] \psi_i = \varepsilon_i \psi_i \tag{2.1.12}$$

$$\rho(\boldsymbol{r}) = \sum_{i=1}^{N} \sum_{s} |\psi_i(\boldsymbol{r}, s)|^2 \tag{2.1.13}$$

where T_s is the KS kinetic energy, v_{eff} is the constructed KS effective potential, v_{xc} is the exchange-correlation potential and ψ_i and ε_i are the N lowest eigenstates and energy eigenvalues of the Schrödinger equation for a single electron moving in v_{eff} and s is the spin orientation $(\uparrow, \downarrow)$.

The KS equations are solved self-consistently by making an initial guess of $\rho(\boldsymbol{r})$ from

[3]Notation here follows Parr [27]: The total energy of the system can be written as

$$E[\rho] = T_s[\rho] + J[\rho] + E_{xc}[\rho] + \int d\boldsymbol{r}\ \rho(\boldsymbol{r}) v(\boldsymbol{r}) \tag{2.1.7}$$

where $v(\boldsymbol{r})$ is the potential due to the placement of the atomic nuclei and any applied external field. $E_{xc}[\rho]$ is the exchange-correlation energy and is defined by

$$E_{xc}[\rho] \equiv T[\rho] - T_s[\rho] + V_{ee}[\rho] - J[\rho] \tag{2.1.8}$$

where T and V_{ee} are the kinetic and potential energies of the interacting electrons and T_s and J are the classical or non-interacting components.

which v_{eff} is found via (2.1.10) and then a new $\rho(\boldsymbol{r})$ is found from (2.1.12) and (2.1.13). Once the difference in density between iterations converges to within some tolerance the ground state is said to be found. The total energy for a given density is calculated from (2.1.7).

In the Kohn-Sham construction the only approximation required is in the exchange-correlation functional as it is not known precisely. If E_{xc} and therefore v_{xc} were known the KS equations would yield ρ exactly, unlike Hartree-Fock which is approximate by nature. The approximation of E_{xc} is a subject of continuous research and experimentation [27, p.142-148].

The popular exchange-correlation functional $B3LYP$ is used in the following report [32–35].

2.1.4 Basis sets

The basis set is a set of orthonormal functions that are used to describe the shape of the atomic orbitals, i.e single electron wave functions. A linear combination of these atomic orbitals form the molecular orbitals. There are various ways to construct the desired basis set, as an example from [36, p.208] a minimal basis set can be constructed for the Hydrogen molecule ion H_2^+ by using a single $1s$ orbital centred on each H nuclei. A minimal basis set uses only atomic orbitals that are occupied in the separated atoms prior to molecular bonding.

For this project, polarizable orbitals $6-311G^{**}$ have been employed. The name is an acronym for the 6 Gaussian type orbitals used to represent the core electrons and the valence is split into three, one and one Gaussian type orbitals respectively. Broader Gaussians are then used to allow for further interaction and polarization denoted by the ** [35]. This basis set is used for three reasons. Firstly, as bonds are formed or as other atoms approach, the shape of atomic orbitals can be altered such as stretching, compressing, shifting etc. Secondly, with increasing applied field one would expect a distortion or further polarization of the atomic orbitals. Thirdly, this is a common basis set that has been used with success when dealing with the process of field evaporation.

For computational speed a pseudopotential basis set $LANL2DZ$ was also used both as a check and initial exploration of desired structures. It should be clear that the final energy calculated via DFT is completely dependent on the basis set employed. The interest here is not necessarily in absolute energy but changes in energy along with other features of the field evaporation process. With these features in mind there is strong agreement between trends seen using these two basis sets for our given models. Elaboration on the use of basis sets in computational chemistry can be found in [35, ch.5] and [37, ch.6].

2.1.5 Geometry optimization

The commercial software package Gaussian09 [38] is used for all density functional calculations. For a given structure, or input of nuclear positions Gaussian calculates the electron density and thus the energy self-consistently using DFT. However to find the the ground state structure not only the electron density but the position of the nuclei must be varied, this is the optimization process.

To begin optimization an initial guess of the structure is made. Gaussian calculates the energy of the structure then shifts the positions of the nuclei and recalculates the energy. At each iteration, the choice of which atoms to shift and in what manner is not done randomly. Both the gradient and Hessian of the energy are considered to make a next guess of step size and direction. The gradient gives the rate of change of the energy surface and the Hessian is a matrix of second order partial derivatives giving information of the concavity. This can be understood as the second and third terms in a Taylor expansion of the energy in many variables [39, p 162],

$$E(\boldsymbol{x}) = E(\boldsymbol{x}_0) + \sum_i \frac{\partial E}{\partial x_i}(x_i - x_{i_0}) + \frac{1}{2}\sum_i \sum_j \frac{\partial^2 E}{\partial x_i \partial x_j}(x_i - x_{i_0})(x_j - x_{j_0}) + \dots \quad (2.1.14)$$

The optimization will step along the energy surface until convergence based on some tolerance is reached. The convergence criteria are the maximum force on a given nuclei $\boldsymbol{F} = -\nabla E$, root-mean-squared (RMS) force $|\boldsymbol{F}| = \sqrt{\sum_i^n F_i^2/n}$, max displacement of an atom computed for the next iteration $(r_{i+1} - r_i)$ and RMS displacement $|r_{i+1} - r_i|/\sqrt{n}$. Once all of these computed values are less than the given thresholds the optimization is said to have converged. Standard values for these convergence criteria are: 0.00045 Ha/Bohr, 0.0003 Ha/Bohr, 0.0018 Å and 0.0012 Å respectively, which can be adjusted as required. Further information on the optimization process can be found on the Gaussian web page.

The geometry optimization is heavily dependent on the initial input structure. As such it may converge in a local minimum on the PE surface. This defines a conformer of the structure with higher energy than the global minimum.

2.2 Field evaporation of polymers

The SAMs of interest in the experimental study by Stoffers, Oberdorfer and Schmitz [1] were made from either perfluoro-decanethiol $CF_3(CF_2)_7(CH_2)_2SH$ or amino-undecanethiol $NH_3(CH_2)_{11}SH$ [4]. The focus here is on the fluorinated SAM as the experimental results were more reliable as noted by the authors.

This is a somewhat ambitious starting point both for the experimentalist and theorist as polymers can be made up of several different elements all with different evaporation field

[4] Hydrogen cleaves from the thiol group so that a strong thiolate ($S-$metal) bond can form, as such thiolate is addressed here.

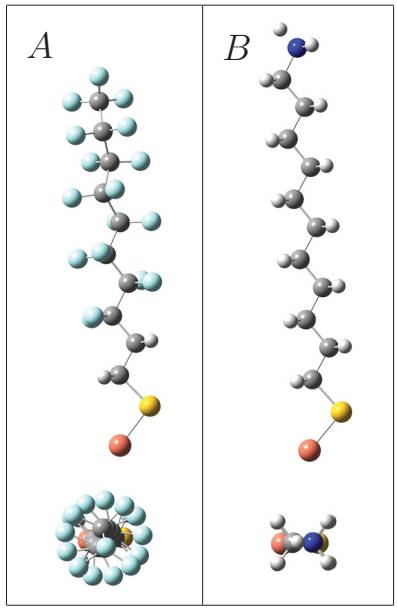

Figure 2.1: Zero field structures for (A) helical perfluoro-decanethiolate and (B) all-trans amino-undecanethiolate adsorbed on Cu. Colouring of atoms, F= light blue, C= grey, H= white, S= yellow, Cu= red, N= dark blue.

strengths. Furthermore, due to the variety of elements there is an increased number of possible molecular fractions that have some probability of evaporating, as compared to a single- or two-element system.

The model studied here is that of a single polymer adsorbed to either a single copper atom or three copper atoms. The larger base provides more space for electrons conducted down the polymer at the point of field evaporation. In this study first the ground state structure in zero applied electric field is found. Then the applied electric field is increased and the geometry optimization is continued until field evaporation sets in. When the applied field pulls a positive ion from the polymer the remaining structure is left with a negative charge. This negative charge is neutralized and the ion removed from subsequent calculations. This is done manually in our calculations or in the form of a current in the experiment. The process is then continued to find the next field evaporated species. As with all simulations a larger more realistic sample is desired. This work should provide the desired jumping off point for future studies using more accurate and intensive models.

2.2.1 Perfluoro-decanethiolate in an applied electric field

DFT calculations were carried out using exchange correlation potential and basis set B3LYP/6-311G**. A metal atom is required in these calculations as an electron sink, for this purpose copper was chosen. The copper atoms in these calculations were held fixed to prevent the structure from drifting in the applied electric field.

Perfluoro-decanethiolate as a single chain attached to a copper atom was found to be helical in its lowest energy state, shown in Figure 2.1. As an initial guess for the nuclear positions an all-trans structure was chosen, i.e. no rotation in the polymer components.

This structure remains stable in fields up to 1 V/Å at which point evaporation sets in. Head group evaporation occurs at 1 V/Å with the removal of CF_3^+. Next, at 1.5 V/Å two groups of $(CF_2)_2^{2+}$ are removed, one after the other. Then at 1.8 V/Å another $(CF_2)_2^{2+}$ is field evaporated followed by the remaining $CF_2(CH_2)_2$ before 2.5 V/Å. The sulphur requires fields close to 5 V/Å to be pulled from the fixed three copper atoms. The first two field evaporated species and field evaporation of sulphur were tested using the larger Cu_3 base model and show the same trend, Figure 2.2.

Three main structural changes occur before evaporation: (1) decrease in polymer tilt angle with respect to the field axis, (2) electrostriction (compression and stretching) along the field axis and (3) a decrease in the coil of the helical structure.

When a field is applied to a SAM the induced polarization causes a torque on the tilted polymers which aligns them with the field. At the same time the polymers are stretched allowing sufficient space for the atoms in this vertical configuration.

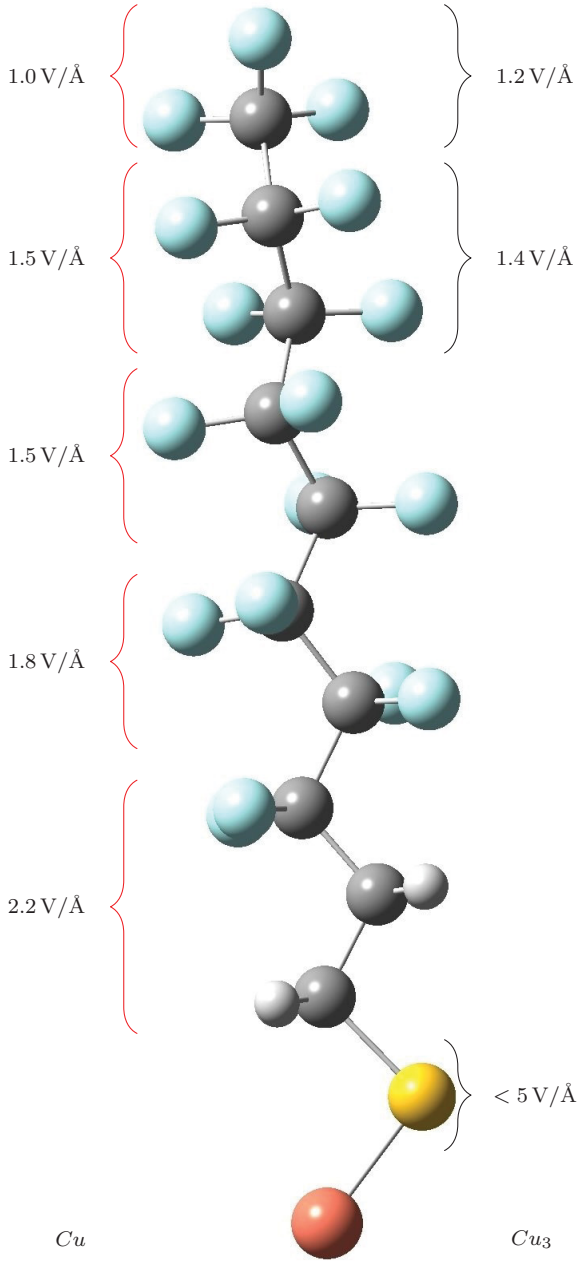

Figure 2.2: Evaporated species from perfluoro-decanethiolate. Applied electric field values are quoted for the model using a single copper base (Cu) and a three copper base (Cu_3).

Using only a single copper atom, there is neither surface nor neighbouring polymer interactions, this is not sufficient to study the effect of an applied field on the angle the polymer makes with the adsorbing metal surface. Because of this, the change in angle with increasing applied field is only few degrees which corresponds to how far the polymer is from the field axis when no field is applied. Using three copper atoms as an electron sink at the base, the polymer is attracted to the

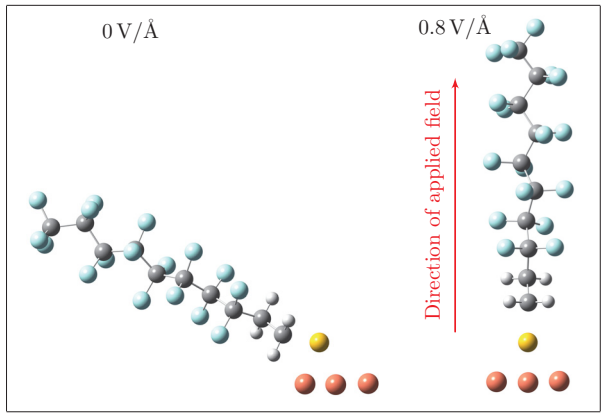

Figure 2.3: Effect of applying a field to a tilted polymer. The polymer here is perfluoro-decanethiolate adsorbed to a three copper base (Cu_3).

surface thus showing a strong tilt in small fields. The polymer is however easily aligned with the applied field before evaporation, Figure 2.3.

If we think of an idealized monolayer with no imperfections in zero applied electric field, then in the central region the polymers will be packed, all executing the same angle with the adsorbing surface. At the edge of the monolayer the angle the polymers make with the adsorbing surface will change, due to the strong repulsion between like charges. As such the polymers at the edge of the monolayer will lean outward from the bulk with the last row of edge polymers laying flat on the metal surface with the head group pointing away from the monolayer. Now taking this system and applying an electric field perpendicular and away from the metal surface, electrons in the polymers are pulled towards the metal surface. At fields of the order of volts per angstrom this transfer of charge is significant making the head groups positively charged. This causes a torque that acts to align the polymers with the field axis. Because of this, at these extreme electric fields the edge polymers lift off of the metal surface and attempt to align with the field axis. Even still the strong repulsion of like charges, mostly due to the electron pairs of the electronegative fluorine in our case, prevents the edge polymers from aligning perfectly with the field axis. As such the edge polymers standing away from the monolayer, unshielded by the bulk, are the location of first evaporation. This of course agrees with the known trends of field evaporation happening first at protrusions and imperfections sites on the surface. This straightening is seen in calculations using three polymers with nine copper atoms in a (111) lattice. Given here are results for the field evaporation on perfluoro-decanethiolate studied as a single polymer standing alone. Due to the above argument and the favourable agreement between initial field evaporation given here and in the experiment, this model well represents the lone polymers at the edge or imperfection sites standing away from the bulk where field evaporation begins.

Electrostriction was seen leading up to the point of field evaporation. Before evaporation of the terminal CF_3 the distance between the copper and terminal carbon atom is first

compressed by 0.2 Å then stretched by nearly 0.7 Å before evaporation, as seen in Figure 2.4. The initial compression of the chain is an interesting phenomenon that is due to the electronegativity of the fluorine groups. Fluorine, being unwilling to give up electrons holds them near at fields below 0.6 V/Å. This causes the electric field to push the fluorine and the polymer as a whole towards the surface. Higher fields cause charge transfer to occur leading to stretching before evaporation. An extreme case of initial compression was observed by Wang et al. [40] in the study of ethylene glycol.

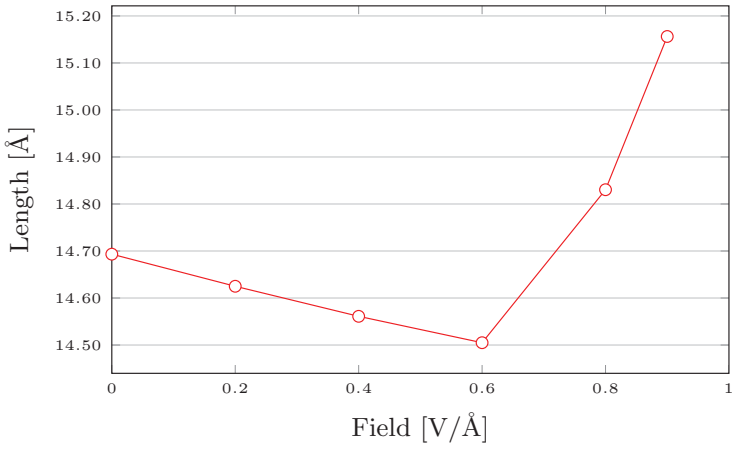

Figure 2.4: Electrostriction experienced by perfluoro-decanethiolate. Length is between terminal carbon and the copper base atom.

As one complete rotation of the helical structure is not achieved over the length of the chain, we can define an angle θ between the two lines connecting $Cu - S$ and the terminal $C - C$ in the x-y plane. This angle is zero for an all-trans structure. The decrease in θ leading up to field evaporation, i.e. from $0 - 0.9$ V/Å, was 18°.

To better understand the movement of charge in the chain, the dipole moment, electric polarizability and dielectric constant have been studied. The single and three copper base is a limitation of this model as it provides a minimal sink for electrons pushed down the chain. As a result, unwanted Coulomb repulsion forces exist in the lower end of the chain at the point of evaporation, i.e. electrons accumulate at the base of the structure. This could act to decrease the dipole moment as a function of the field as it becomes increasingly difficult for charge to transfer down the chain. It is clear from the increasing dipole moment that these effects are not dominant in the single polymer model for perfluoro-decanethiolate, see Figure 2.5.

Fluorine being highly electronegative causes a negative dipole moment at fields below 0.4 V/Å. The dipole moment is however reversed at higher fields. There appears to exist two regimes, (1) below 0.6 V/Å minimal charge transfer is accomplished by the field, (2) above 0.6 V/Å the electric field overcomes the electronegativity of the chain pulling charge down the chain until evaporation at > 0.9 V/Å. Region (1) and (2) correspond to the compression

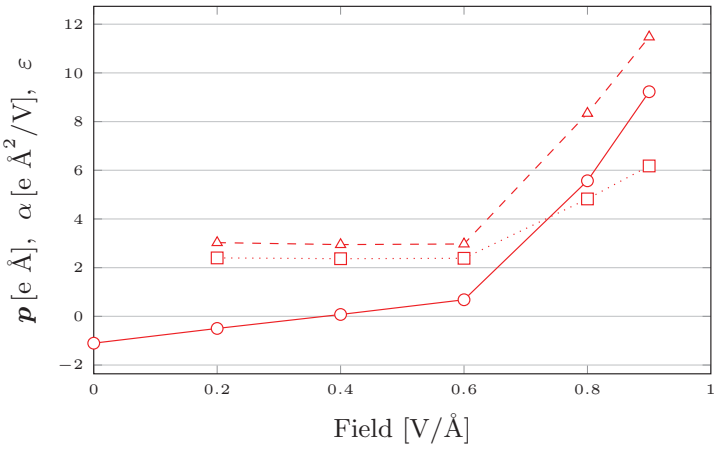

Figure 2.5: Solid circle: dipole moment $\boldsymbol{p}$ [eÅ] along the field axis (+z) of perfluoro-decanethiolate. Dashed triangle: electric polarizability α [eÅ^2/V]. Dotted square: dielectric constant ε.

and stretching stages respectively. This is also reflected in the trend of induced electric polarizability $\alpha = p/E$ and dielectric constant given by $\varepsilon = 1 + \alpha/(\varepsilon_0 V)$, where V is the volume occupied by the chain given by a cylinder around the polymer of length and width given by the nuclear positions plus the Bohr radius. We note that the dielectric constant $\varepsilon = 2.3$ from this calculation is close to that expected for alkane-like chains. These trends agree with the electrostriction mentioned above.

Given the length of the polymer d and the dipole moment p we can calculate the effective charge $q = p/d$ transferred over the length of the chain, which is on the order of $0.6\,e$ before evaporation.

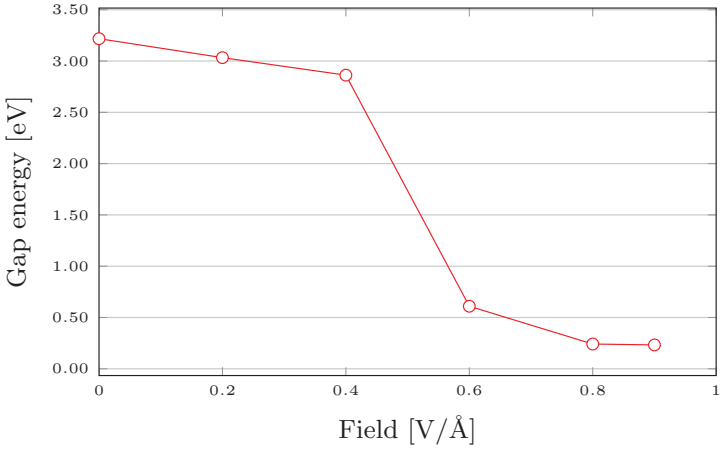

Figure 2.6: HOMO/LUMO gap of perfluoro-decanethiolate in an applied electric field until evaporation.

Plotted in Figure 2.6 is the HOMO/LUMO gap for perfluoro-decanethiolate showing the expected decrease before evaporation [16–20], eventually becoming zero. We expect evaporation to coincide with this drop in the HOMO/LUMO gap energy as this would correspond to the most vulnerable state at which the applied field can most easily create charge separation within the polymer, this is of course confirmed with the increased polarizability.

2.2.2 Amino-undecanethiolate in an applied electric field

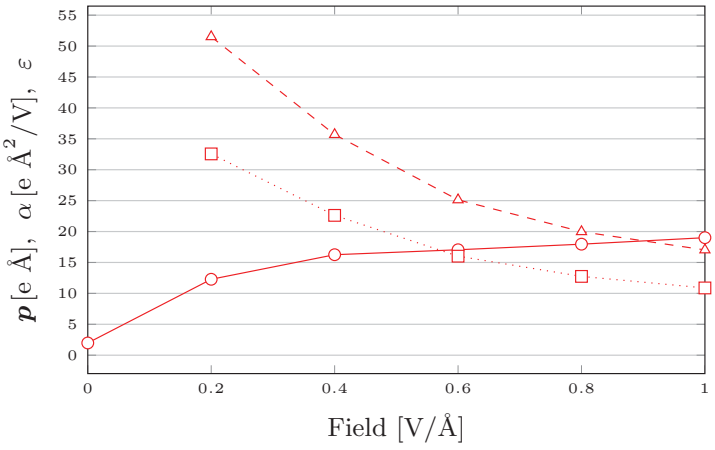

Figure 2.7: Solid circle: dipole moment $\boldsymbol{p}$ [eÅ] along the field axis (+z) of amino-undecanethiolate. Dashed triangle: electric polarizability α [eÅ^2/V]. Dotted square: dielectric constant ε.

A similar analysis was carried out for amino-undecanethiolate on a Cu atom, which was found to be an all-trans structure in its ground-state, seen in Figure 2.1. The dipole moment in Figure 2.7, shows a diminishing positive slope with increasing field. Charge transfer was on the order of e over the length of the chain before head group evaporation. The polymer did not experience any compression before it stretched 1.1 Å towards evaporation. The angle with the field axis decreased by 2° before evaporation of $NH_3(CH_2)_3^{2+}$ at 1.1 V/Å. Next evaporation occurred at 1.5 V/Å with the removal of two groups of $(CH_2)_2^{2+}$, Figure 2.8. The evaporated species found in the three copper base model were $NH_3(CH_2)_2^{2+}$ at 1.2 V/Å. Next evaporation occurred at 1.4 V/Å with the removal of $(CH_2)_3^{2+}$ and then $(CH_2)_4^{2+}$ and $(CH_2)_2$ at 1.6 V/Å. The sulphur again required fields close to 5 V/Å, Figure 2.8.

Under experimental conditions the polymer is adsorbed on a metal surface, i.e the atom probe tip. When evaporation occurs the positive evaporated ion is pulled towards the detector as the equivalent charge in electrons is conducted down the circuit to recombine. Before evaporation no current flows down the atom probe tip. Electrons transferred to the metal surface by the field are distributed over the conductor in the region of the polymer forming a surface charge, equivalent to the image charge of the polymer.

With the single copper atom at the base, the amino-undecanethiolate model shows a

decreasing positive slope in dipole moment with increasing applied field. In part, this is a result of charge accumulation in the base of the polymer before field evaporation as mentioned above and is reflected in Figure 2.7 by the decreasing slope of dipole moment with increasing field. Allowing the electrons to move away from the base of the chain, as would be the case in experiment, will allow further electron transfer to occur. A larger electron sink is incorporated by the model with a three copper atom base. The dipole moment in this case was indeed increased. Although this model allowed for further electron transfer, the polarizability and dielectric constant showed similar decreasing trends suggesting that charge accumulation is not a dominant factor.

Unlike perfluoro-decanethiolate, amino-undecanethiolate is polarized at low applied fields. The polymer becomes increasingly difficult to further polarize due to (1) electronegativity of the amino group and (2) the charge separation that has already occurred at lower applied fields, Figure 2.7. As mentioned earlier the electronegativity in the case of perfluoro-decanethiolate is only overcome at high fields thus the trends in α are completely different.

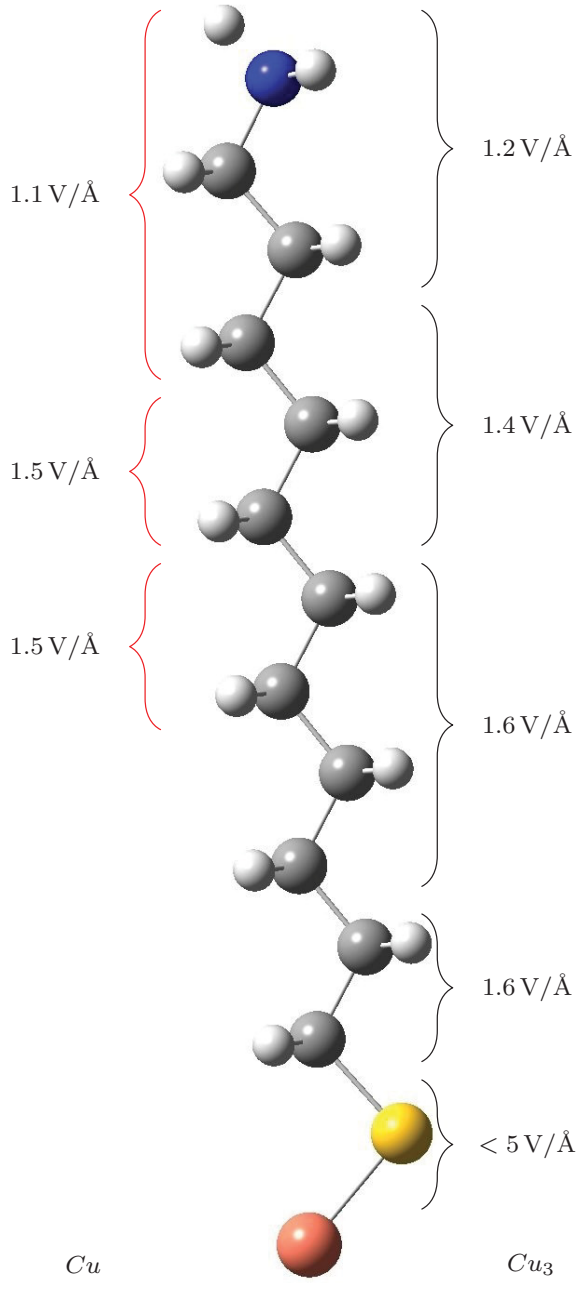

Figure 2.8: Evaporated species from amino-undecanethiolate. Applied electric field values are quoted for the model using a single copper base (Cu) and a three copper base (Cu_3).

2.2.3 Comparison with Experiment

For the evaporation of perfluoro-decanethiolate given in [1] CF_3^+ (and $C_2F_4^+$), F^+, $SC_9F_4^+$ evaporate at $1.0 - 1.2$, $2.0 - 3.0$, and $3.5 - 4.0$ V/Å respectively. As shown in the above results there is agreement for the field required to evaporate the first CF_3 group and the following C_2F_4 groups. There was no indication in these calculations that the large $SC_9F_4^+$ group field evaporates. Field evaporation

is a time dependent process, and the use of a laser to initiate field evaporation is not included in these calculations. As such the evaporation fractions seen in this time independent DFT model are not the only possibilities. Even still it is surprising that $SC_9F_4^+$ is seen as a dominant fraction as opposed to the small fluorocarbon fractions in this study. It is possible that as the length of the polymers decrease the single polymer model becomes less representative of the evaporation process. As noted earlier, the evaporation process starts at edges and imperfections where polymers are more exposed to the electric field. As the length of the polymers decrease the head groups at edges are less exposed to the field, hence, the effect of the bulk becomes more important. Further theoretical and experimental testing is required to understand the evaporation process of this SAM.

In [1] it is noted that the amino-undecanethiol data is less convincing due to the presence of excess hydrogen and oxygen in the atom probe chamber leading to larger error in the mass spectrum analysis. From the single polymer model presented here, evaporation of $NH_3(CH_2)_3^{2+}$ was found to be at 1.1 V/Å. Stoffers analysis shows only groups of the form OH_x appearing at such low voltages. There should be a difference between the theoretical single polymer in a uniform field and the experimental dense dielectric. In a dielectric, such as a SAM, the field is reduced in the interior and enhanced at the surface. Thus the field strength to break internal bonds should be larger for the experimental SAM when comparing with our single polymer model. Considering the strong agreement between the model and experiment for initial evaporation of perfluoro-decanethiolate, it is surprising that the evaporation field strength for amino-decanethiolate is so high compared to its single polymer model. With the contrasting trends in charge transfer between these polymers we should not necessarily expect similar results. Further research in this area is definitely of interest.

2.3 Summary

This DFT study was able to successfully reproduce initial field evaporation of the fluorinated polymer perfluoro-decanethiolate. Expected trends that agree with current literature, such as that seen for the HOMO/LUMO gap were observed. Other trends such as electrostriction and charge transfer where studied showing the interesting compression characteristic of polymers with electronegative groups. This offers the major contrasting point between the two polymers, perfluoro-decanethiolate being dominated by the electronegative fluorine groups causing compression and amino-undecanethiolate not experiencing any compression.

3. Kinetics of field evaporation

Density functional theory has become the standard method of studying physical systems at the atomic and molecular level. Applying this theory to structures in electric fields on the order of volts per angstrom has given results that form the cornerstone of our theoretical understanding and investigation in the area of field evaporation. Even though it is well established DFT is still an area of intense research making its use more widely applicable. The issue with density functional theory is that it is fundamentally a ground state theory and therein lies its limitations. When studying field evaporation we would like to know not only the most probable evaporation species but a comparison between a variety of species at the same applied electric field. Furthermore, the relevance of time cannot be understood with the current time independent models. For this we must employ other methods of calculation.

To study the kinetics of the field evaporation process we consider a model system of a protruding atom from an otherwise smooth surface. The bulk is assumed to be made up of a statistical size sample of particles such that we can define a temperature [41]. Due to the finite temperature of the system there are thermal vibrations, or phonon modes that are set up in the bulk, these phonons are available to transfer thermal vibrational energy to the surface atom. Therefore, the phonons allow for the surface atom to randomly sample all of the possible vibrational bound states allowed by the finite temperature of the bulk. Occupation of such vibrational levels is thus given by the Boltzmann factor.

In a most general form, we would like to know the rate of field evaporation of this surface atom or molecule under the influence of an applied electric field. For this we first look at the cause of field evaporation from the view point of the electron.

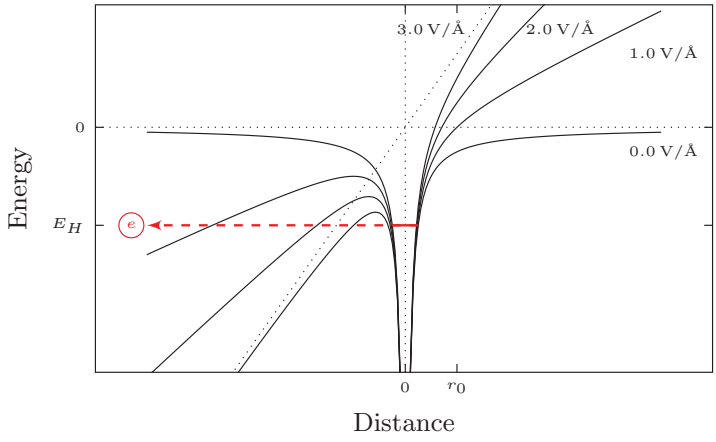

Figure 3.1: Coulomb style potential with applied homogeneous electric field for an atom of radius r_0 showing the electron tunnelling out of the atom from the highest occupied level E_H.

For field evaporation to occur, surface atoms must become ionized. Once ionized, the

force away from the surface due to the electric field is so great that field evaporation takes place. Ionization of surface atoms is the result of electron tunnelling. In an applied electric field, electrons move with a potential energy of the form

$$V \approx -\frac{1}{4\pi\varepsilon_0}\frac{Qe}{z} + e\tilde{E}z \tag{3.0.1}$$

which is the sum of terms relating to the coulomb atomic potential and linear applied potential where Q is the effective ionic charge and $\tilde{E}$ is the applied electric field. Plotting this for a range of electric fields, Figure 3.1, it is clear that the barrier to the left decreases with increasing field. As a result electrons can tunnel out of the atomic potential easier at higher applied electric fields.

Calculating the rate of field evaporation in this electron focused picture amounts to calculating the time it takes for an electron in the highest occupied orbital of the atom to tunnel into the bulk. There are several common approximations[1] for this, the most simplistic being the Buttiker-Landauer time [46]

$$\begin{aligned} t &= \int dz\, \frac{1}{v} = \int dz\, \frac{m}{p} \\ &= \int dz\, \frac{m}{\sqrt{2m(E - V(z))}} \\ \tau_{BL} &= \int dz \sqrt{\frac{m}{2(E - V(z))}} \end{aligned} \tag{3.0.2}$$

where integration is over the barrier region where $E < V(z)$. Regardless of the approximation used for the tunnelling time this is the crudest approximation to the rate of field evaporation. The reason for this is we can only calculate ground state information using density functional theory. As such, if an atom is in some excited vibrational state we do not know how the potential energy, $V(z)$, the electron sees is affected[2]. Hence we can only calculate an approximation to the tunnelling time using a calculation of the ground state potential energy.

Alternatively, we can look at this problem from the perspective of the nucleus, where we are interested in making a transition from an initial bound state to a final free ionic state. The solution to this problem can be formulated in terms of transition rates with the use of Fermi's Golden Rule [25, ch.6][47, ch.7]. The probability of making a transition per unit time between some initial state with wave function ψ_i and some final state with ψ_f connected by

[1] Electron tunnelling time has been and is still the centre of much debate, τ_{BL} is an imaginary time for example, see [42–45] for some past and current reviews of competing theories and recent experimental efforts with attoclock measurements. Also [25, p.295] for the solution to the hydrogen atom.

[2] With nonzero motion of the atom with respect to the surface the tunnelling barrier fluctuates in size and shape.

an interaction potential energy V_{fi} is given to be[3]

$$T_{fi} = \frac{2\pi}{\hbar} \left| \int d\boldsymbol{r} \psi_f^*(\boldsymbol{r}) V_{fi}(\boldsymbol{r}) \psi_i(\boldsymbol{r}) \right|^2 \delta(E_f - E_i - E_t) \tag{3.0.3}$$

where E_i, E_f are the energies of initial and final states, E_t is some externally supplied energy. If there is no source of energy E_t to make a transition from $\psi_i \to \psi_f$ than the transition will only happen if the initial energy is equal to the final energy, hence, the delta function is the result of conservation of energy[4].

To find the total transition rate from a group of initial states $\psi_{i\nu}$ to a group of final states $\psi_{f\mu}$ we sum the contributions of each transition weighed by the probability that the initial state is occupied and the final state is not.

In this picture, the rate of field evaporation can be calculated including temperature effects unlike the previous case. Density functional theory provides a method to calculate the surface potential that the atom exists in and all excited vibrational states can be found from this. This is all that is required to pursue the rate of field evaporation in this nuclear picture. The derivation for transitions leading to field evaporation in this picture will be developed in the following sections culminating in the finial equation for the rate of field evaporation of a given species.

3.1 Theoretical construction

We wish to understand the field evaporation of surface particles, both atomic and molecular. In atom probe experiments the evaporated particles are those at edges, protruding in someway from the surface. As a model we assume a flat surface with a particle sitting on top. Note this surface particle can be of any form, atomic or molecular, and represents the species that will be field evaporated. This general surface particle will be referred to as the adparticle, and due to a lack of nomenclature, the sum of the nuclei making up the adparticle will be referred to as the adparticle nucleus. This section follows closely with [2], more detail will be shown in relevant sections and citations given.

To start we will only consider the energy levels in which the adparticle can exist, no kinetics such as rate of change of occupation of these levels. As such, for the moment we neglect energy transfer from phonons of the bulk to the adparticle, hence, we ignore the kinetic energy of the bulk atoms by keeping them fixed. The Hamiltonian of this system is

[3]Here, wave functions ψ_i, ψ_f are assumed to be bound and therefore normalized by $\int dr \psi^* \psi = 1$. Hence, the units of the wave functions are $[\boldsymbol{r}]^{-1/2}$ giving the units of T as $[s]^{-1}$. In the case of transitions between (1) bound and un-bound or continuous states and (2) between continuous states, this equation cannot be directly interpreted as a rate as the dimensions of T will depend on the normalization of the continuum wave functions [25, §43].

[4]It must be understood that this delta function representation (3.0.3) only holds meaning if there is a dense set of final states to transition into. The delta function is thus lost upon integration over the final states, $\int df\, g_f T_{fi}$, introducing the density of states function g_f of the final states. If the final states are not degenerate than $df\, g_f \to dE\, g_f(E)$.

then given by

$$\hat{H}_a = \hat{T}_N + \hat{H}_e(\boldsymbol{r}_1, \boldsymbol{r}_2, \ldots; \boldsymbol{R}) \tag{3.1.1}$$

where $\boldsymbol{r}_n$ and $\boldsymbol{R}$ are the positions of the electrons and adparticle nucleus respectively,

$$\hat{T}_N = -\frac{\hbar^2}{2M}\nabla^2_{\boldsymbol{R}} \tag{3.1.2}$$

is the kinetic energy of the adparticle nucleus

$$\hat{H}_e = -\frac{\hbar}{2m}\sum_n \nabla^2_n + V_e(\boldsymbol{r}_1, \boldsymbol{r}_2, \ldots; \boldsymbol{R}) \tag{3.1.3}$$

is the electronic Hamiltonian where V_e includes Coulomb interactions between electrons, electrons and the adparticle nuclei, and between all nuclei (adparticle and surface), hence this includes any applied potential.

3.1.1 Adiabatic states

Adiabatic states are given by the Born-Oppenheimer approximation, where it is assumed that $\boldsymbol{R}$, the position of the adparticle nucleus, is slowly varying in comparison to the electrons positions, $\boldsymbol{r}$. In such a case the electrons have time to adjust to changes in nuclear geometry. These states can be calculated using density functional theory.

The many electron eigenfunctions $\zeta_i(\boldsymbol{r}; \boldsymbol{R})$ of the electronic Hamiltonian represent adiabatic states

$$\hat{H}_e(\boldsymbol{r}; \boldsymbol{R})\zeta_i(\boldsymbol{r}; \boldsymbol{R}) = V_i(\boldsymbol{R})\zeta_i(\boldsymbol{r}; \boldsymbol{R}). \tag{3.1.4}$$

where $\boldsymbol{r}$ represents the N electron coordinates $\boldsymbol{r}_1, \boldsymbol{r}_2, \ldots, \boldsymbol{r}_N$ and eigenvalues V_i are the potential energy states where V_0 and V_1 are the ground state and first electronically excited adiabatic state respectively.

Operator matrices are put in diagonal form if expanded using their eigenfunctions[5]. Eigenfunctions of $\hat{H}_a$ have the property

$$\hat{H}_a\Psi_\alpha = E_\alpha\Psi_\alpha \tag{3.1.5}$$

[5]Landau §11: Dirac notation for matrix element

$$f_{nm} \equiv \langle n|f|m\rangle = \int \psi^*_n f \psi_m dq$$

$$\langle n|m\rangle = \int \psi^*_n \psi_m dq$$

we attempt a solution in the form of a linear combination of adiabatic eigenfunctions

$$\Psi_\alpha(\boldsymbol{r};\boldsymbol{R}) = \sum_i \zeta_i(\boldsymbol{r};\boldsymbol{R})\chi_{i\alpha}(\boldsymbol{R}) \tag{3.1.6}$$

where $\chi_{i\alpha}(\boldsymbol{R})$ is the adiabatic eigenfunction of the adparticle nucleus. Looking first at the LHS of (3.1.5) after multiplying by $\zeta_i^*(\boldsymbol{r};\boldsymbol{R})$ and integrating over all electron coordinates,

$$\int_{\boldsymbol{r}} d\boldsymbol{r}\zeta_i^*(\boldsymbol{r};\boldsymbol{R})\hat{H}_a\Psi_\alpha(\boldsymbol{r};\boldsymbol{R}) \;=\; \int_{\boldsymbol{r}} d\boldsymbol{r}\zeta_i^*(\boldsymbol{r};\boldsymbol{R})\hat{T}_N\Psi_\alpha(\boldsymbol{r};\boldsymbol{R}) + \int_{\boldsymbol{r}} d\boldsymbol{r}\zeta_i^*(\boldsymbol{r};\boldsymbol{R})\hat{H}_e\Psi_\alpha(\boldsymbol{r};\boldsymbol{R}). \tag{3.1.7}$$

Considering the first term,

$$\begin{aligned}\hat{T}_N\Psi_\alpha(\boldsymbol{r};\boldsymbol{R}) &= -\frac{\hbar^2}{2M}\left[2\sum_i \frac{\partial\zeta_i(\boldsymbol{r};\boldsymbol{R})}{\partial\boldsymbol{R}}\frac{\partial\chi_{i\alpha}(\boldsymbol{R})}{\partial\boldsymbol{R}}\right.\\ &\quad + \sum_i \frac{\partial^2\zeta_i(\boldsymbol{r};\boldsymbol{R})}{\partial\boldsymbol{R}^2}\chi_{i\alpha}(\boldsymbol{R})\\ &\quad \left. + \sum_i \zeta_i(\boldsymbol{r};\boldsymbol{R})\frac{\partial^2\chi_{i\alpha}(\boldsymbol{R})}{\partial\boldsymbol{R}^2}\right],\end{aligned} \tag{3.1.8}$$

$$\begin{aligned}\int_{\boldsymbol{r}} d\boldsymbol{r}\zeta_i^*(\boldsymbol{r};\boldsymbol{R})\hat{T}_N\Psi_\alpha(\boldsymbol{r};\boldsymbol{R}) &= -\frac{\hbar^2}{2M}\left[2\int_{\boldsymbol{r}} d\boldsymbol{r}\zeta_i^*(\boldsymbol{r};\boldsymbol{R})\sum_j \frac{\partial\zeta_j(\boldsymbol{r};\boldsymbol{R})}{\partial\boldsymbol{R}}\frac{\partial\chi_{j\alpha}(\boldsymbol{R})}{\partial\boldsymbol{R}}\right.\\ &\quad + \int_{\boldsymbol{r}} d\boldsymbol{r}\zeta_i^*(\boldsymbol{r};\boldsymbol{R})\sum_j \frac{\partial^2\zeta_j(\boldsymbol{r};\boldsymbol{R})}{\partial\boldsymbol{R}^2}\chi_{j\alpha}(\boldsymbol{R})\\ &\quad \left. + \int_{\boldsymbol{r}} d\boldsymbol{r}\zeta_i^*(\boldsymbol{r};\boldsymbol{R})\sum_j \zeta_j(\boldsymbol{r};\boldsymbol{R})\frac{\partial^2\chi_{j\alpha}(\boldsymbol{R})}{\partial\boldsymbol{R}^2}\right]\end{aligned} \tag{3.1.9}$$

$$\begin{aligned}&= -\frac{\hbar^2}{2M}\left[2\sum_j D_{ij}^{(1)}\frac{\partial\chi_{j\alpha}(\boldsymbol{R})}{\partial\boldsymbol{R}}\right.\\ &\quad \left. + \sum_j D_{ij}^{(2)}\chi_{j\alpha}(\boldsymbol{R}) + \frac{\partial^2\chi_{i\alpha}(\boldsymbol{R})}{\partial\boldsymbol{R}^2}\right]\end{aligned} \tag{3.1.10}$$

$$D_{ij}^{(1)}(\boldsymbol{R}) = \int_{\boldsymbol{r}} d\boldsymbol{r}\zeta_i^*(\boldsymbol{r};\boldsymbol{R})\frac{\partial\zeta_j(\boldsymbol{r};\boldsymbol{R})}{\partial\boldsymbol{R}} \tag{3.1.11}$$

$$D_{ij}^{(2)}(\boldsymbol{R}) = \int_{\boldsymbol{r}} d\boldsymbol{r}\zeta_i^*(\boldsymbol{r};\boldsymbol{R})\frac{\partial^2\zeta_j(\boldsymbol{r};\boldsymbol{R})}{\partial\boldsymbol{R}^2}. \tag{3.1.12}$$

Considering the second term[6],

$$\begin{aligned}\int_{\boldsymbol{r}} d\boldsymbol{r}\zeta_i^*(\boldsymbol{r};\boldsymbol{R})\hat{H}_e\Psi_\alpha(\boldsymbol{r};\boldsymbol{R}) &= \int_{\boldsymbol{r}} d\boldsymbol{r}\zeta_i^*(\boldsymbol{r};\boldsymbol{R})\sum_j V_j(\boldsymbol{R})\zeta_j(\boldsymbol{r};\boldsymbol{R})\chi_{j\alpha}(\boldsymbol{R}) \\ &= V_i(\boldsymbol{R})\chi_{i\alpha}(\boldsymbol{R}). \end{aligned} \tag{3.1.13}$$

Now for the RHS of (3.1.5)

$$\int_{\boldsymbol{r}} d\boldsymbol{r}\zeta_i(\boldsymbol{r};\boldsymbol{R})^* E_\alpha \sum_j \zeta_j(\boldsymbol{r};\boldsymbol{R})\chi_{j\alpha}(\boldsymbol{R}) = E_\alpha\chi_{i\alpha} \tag{3.1.14}$$

which results in a coupled set of equations

$$\left(-\frac{\hbar^2}{2M}\frac{\partial^2}{\partial\boldsymbol{R}^2} + V_i(\boldsymbol{R}) - E_\alpha\right)\chi_{i\alpha}(\boldsymbol{R}) = \frac{\hbar^2}{2M}\sum_j\left(D_{ij}^{(2)} + 2D_{ij}^{(1)}\frac{\partial}{\partial\boldsymbol{R}}\right)\chi_{j\alpha}. \tag{3.1.15}$$

3.1.2 Diabatic states

Diabatic states are states in which the nuclear positions vary rapidly such that the electrons of a given atom do not have the time to adjust to changes in nuclear position. As such, a diabatic state is a state in which the charge does not change as a function of nuclear position. We are interested in making a transition between adparticle states of different charge, each of these states is given by its own diabatic potential energy function which can be constructed using the adiabatic states.

For this we introduce a set of new diabatic nuclear states $\boldsymbol{\eta}$ which relate to the adiabatic nuclear states, $\boldsymbol{\chi}^T = (\chi_1, \chi_2, \ldots)$, via unitary transformation A [25, §12],

$$\boldsymbol{\chi} = A\boldsymbol{\eta} \tag{3.1.16}$$

A is an explicit function of the nuclear position. Substituting $\chi_{i\alpha}(\boldsymbol{R}) = A\eta_{i\alpha}(\boldsymbol{R})$ into (3.1.15) results in,

$$\left(-\frac{\hbar^2}{2M}\frac{\partial^2}{\partial\boldsymbol{R}^2} + V_i(\boldsymbol{R}) - E_\alpha\right)A\eta_{i\alpha}(\boldsymbol{R}) = \frac{\hbar^2}{2M}\sum_j\left(D_{ij}^{(2)} + 2D_{ij}^{(1)}\frac{\partial}{\partial\boldsymbol{R}}\right)A\eta_{j\alpha}. \tag{3.1.17}$$

A must satisfy

$$\left(\frac{\partial}{\partial\boldsymbol{R}} + D^{(1)}\right)A = 0 \tag{3.1.18}$$

to eliminate any coupling between the adiabatic and diabatic states in the final solution [48–

[6] Using again the orthogonality of the wave functions

$$\int_r d\boldsymbol{r}\,\zeta_i^*\zeta_j = \delta_{ij}$$

where $\boldsymbol{r}$ is dependent on $3N$ spatial variables where N is the number of electrons and $d\boldsymbol{r} = d\boldsymbol{r}_1\, d\boldsymbol{r}_2 \ldots d\boldsymbol{r}_N$.

50], hence giving a strictly diabatic solution. Taking the derivative of (3.1.18) with respect to $\boldsymbol{R}$ gives

$$\frac{\partial^2 A}{\partial \boldsymbol{R}^2} + \frac{\partial D^{(1)}}{\partial \boldsymbol{R}} A + D^{(1)} \frac{\partial A}{\partial \boldsymbol{R}} = 0 \tag{3.1.19}$$

The term $\partial D^{(1)}/\partial \boldsymbol{R}$ can be re-expressed as[7]

$$\begin{aligned}
\frac{\partial D^{(1)}}{\partial \boldsymbol{R}} &= \frac{\partial}{\partial \boldsymbol{R}} \langle \zeta_i | \frac{\partial}{\partial \boldsymbol{R}} \zeta_j \rangle \\
&= \langle \frac{\partial}{\partial \boldsymbol{R}} \zeta_i | \frac{\partial}{\partial \boldsymbol{R}} \zeta_j \rangle + \langle \zeta_i | \frac{\partial^2}{\partial \boldsymbol{R}^2} \zeta_j \rangle \\
&= \sum_n \langle \frac{\partial}{\partial \boldsymbol{R}} \zeta_i | \zeta_n \rangle \langle \zeta_n | \frac{\partial}{\partial \boldsymbol{R}} \zeta_j \rangle + \langle \zeta_i | \frac{\partial^2}{\partial \boldsymbol{R}^2} \zeta_j \rangle \\
&= \widetilde{D}^{(1)*} D^{(1)} + D^{(2)}
\end{aligned} \tag{3.1.20}$$

where $\widetilde{D}^{(1)*}$ denotes the complex conjugate of the transpose of $D^{(1)}$.[8] The electronic wave functions are assumed to be real thus $\widetilde{D}^{(1)*} = \widetilde{D}^{(1)}$, and by definition the derivative operator is and antisymmetric matrix giving $\widetilde{D}^{(1)} = -D^{(1)}$ [47, p.125]. Finally,

$$\frac{\partial D^{(1)}}{\partial \boldsymbol{R}} = D^{(2)} - D^{(1)} D^{(1)} \tag{3.1.23}$$

and simplifying (3.1.19) using (3.1.18) and (3.1.23),

$$\frac{\partial^2 A}{\partial \boldsymbol{R}^2} + 2D^{(1)} \frac{\partial A}{\partial \boldsymbol{R}} + D^{(2)} A = 0 \tag{3.1.24}$$

[7] By definition

$$\langle \phi | \hat{f} | \psi \rangle \equiv \langle \phi | \hat{f} \psi \rangle$$

as the operator acts to the right. Here the extra bar is left out for clarity.

[8] Further points in the notation of Dirac

$$\langle \psi_n | \hat{f} \psi_m \rangle = \int dq\, \psi_n^* (\hat{f} \psi_m) = \int dq\, \psi_m (\hat{f}^\dagger \psi_n)^* = \langle \hat{f}^\dagger \psi_n | \psi_m \rangle \tag{3.1.21}$$

If the operator $\hat{f}$ corresponds to values f than the operator $\hat{f}^\dagger \equiv \tilde{\hat{f}}^*$ called the Hermitian conjugate or conjugate transpose of $\hat{f}$ corresponds to values f^*,

$$\begin{gathered}
f_{nm} = \int dq\, \psi_n^* \hat{f} \psi_m = \langle \psi_n | \hat{f} | \psi_m \rangle \\
(f^*)_{nm} = \int dq\, \psi_n^* \hat{f}^\dagger \psi_m = \int dq\, \psi_n^* \tilde{\hat{f}}^* \psi_m = \int dq\, \psi_m \hat{f}^* \psi_n^* = (f_{mn})^* = \langle \psi_n | \hat{f}^\dagger | \psi_m \rangle
\end{gathered} \tag{3.1.22}$$

Rearranging (3.1.17),

$$-\frac{\hbar^2}{2M}\left(\frac{\partial^2}{\partial \boldsymbol{R}^2}A\eta_{i\alpha}+\sum_j\left(D_{ij}^{(2)}+2D_{ij}^{(1)}\frac{\partial}{\partial \boldsymbol{R}}\right)A\eta_{j\alpha}\right)+(V_i-E_\alpha)\,A\eta_{i\alpha}=0 \tag{3.1.25}$$

and expanding results in

$$\begin{aligned}-\frac{\hbar^2}{2M}&\left(\frac{\partial^2 A}{\partial \boldsymbol{R}^2}\eta_{i\alpha}+\sum_j\left(2D_{ij}^{(1)}\frac{\partial A}{\partial \boldsymbol{R}}\eta_{j\alpha}+D_{ij}^{(2)}A\eta_{j\alpha}\right)\right.\\ &\left.+2\left(\frac{\partial A}{\partial \boldsymbol{R}}\frac{\partial \eta_{i\alpha}}{\partial \boldsymbol{R}}+\sum_j D_{ij}^{(1)}A\frac{\partial \eta_{j\alpha}}{\partial \boldsymbol{R}}\right)+A\frac{\partial^2\eta_{i\alpha}}{\partial \boldsymbol{R}^2}\right)+(V_i-E_\alpha)\,A\eta_{i\alpha}=0.\end{aligned} \tag{3.1.26}$$

This can then be simplified using matrix notation[9] and imposing the conditions (3.1.18) and (3.1.24),

$$-\frac{\hbar^2}{2M}A\frac{\partial^2\eta_{i\alpha}}{\partial \boldsymbol{R}^2}+(V_i-E_\alpha)A\eta_{i\alpha}=0. \tag{3.1.27}$$

Finally, multiplying through on the left with the Hermitian conjugate of A, $A^\dagger$ gives,

$$\left(-\frac{\hbar^2}{2M}I\frac{\partial^2}{\partial \boldsymbol{R}^2}+W-EI\right)\eta=0 \tag{3.1.28}$$

where I is the identity matrix and $W=A^\dagger VA$ is the diabatic interaction matrix. The uncoupled diabatic states are therefore given by the diagonal elements of the interaction matrix W

$$\left(-\frac{\hbar^2}{2M}\frac{\partial^2}{\partial \boldsymbol{R}^2}+W_{ii}-E_{i\nu}\right)\eta_{i\nu}^0=0 \tag{3.1.29}$$

where $\eta_{i\nu}^0$ is the ν^{th} eigenstate with energy $E_{i\nu}$ of the i^{th} diabatic potential energy curve $W_{ii}(\boldsymbol{R})$. E.g. W_{00} would be the potential energy of a neutral atom approaching a surface, and W_{11} that of an ion. The off-diagonal terms W_{ij} couple these states together; in the above example, W_{10} is responsible for ionization or neutralization.

[9] Where $D^{(1)}$, $D^{(2)}$ and A are matrices

$$(DA)_{ij}=\sum_k D_{ik}A_{kj}$$

hence, terms such as

$$\sum_j D_{ij}^{(1)}\frac{\partial A}{\partial \boldsymbol{R}}\eta_{j\alpha}=\left(D^{(1)}\frac{\partial A}{\partial \boldsymbol{R}}\eta\right)_{i\alpha}$$

simplify.

We can at this point rewrite the total wave function as

$$\begin{aligned}\Psi_\alpha(\boldsymbol{r};\boldsymbol{R}) &= \sum_i \zeta_i(\boldsymbol{r};\boldsymbol{R})\chi_{i\alpha}(\boldsymbol{R}) \\ &= \sum_i \zeta_i(\boldsymbol{r};\boldsymbol{R})A_{ij}(\boldsymbol{R})\eta_{j\alpha}(\boldsymbol{R}) \\ &= \sum_j \xi_j(\boldsymbol{r};\boldsymbol{R})\eta_{j\alpha}(\boldsymbol{R}) \end{aligned} \tag{3.1.30}$$

where $\xi_j(\boldsymbol{r};\boldsymbol{R})$ is the diabatic many-electron wave function.

3.1.3 Two state system

Now that the relations between adiabatic and diabatic states have been developed, we would like to study the adiabatic process of field ionization from the point of view of diabatic states. We consider a situation where a transition is made between two given diabatic states. More explicitly we are interested in the transition between a particle in a bound state to that of a free ionized particle. The unitary transformation A for a two state system can in general be stated as[10]

$$A = \begin{pmatrix} \cos\theta & \sin\theta \\ -\sin\theta & \cos\theta \end{pmatrix} \tag{3.1.31}$$

here we let θ be a function of $\boldsymbol{R}$ and find its dependence by imposing the condition (3.1.18) where we know from earlier that $D^{(1)}$ is antisymmetric,

$$\begin{aligned}\frac{\partial}{\partial \boldsymbol{R}}\begin{pmatrix} \cos\theta & \sin\theta \\ -\sin\theta & \cos\theta \end{pmatrix} + \begin{pmatrix} 0 & D_{01}^{(1)} \\ -D_{01}^{(1)} & 0 \end{pmatrix}\begin{pmatrix} \cos\theta & \sin\theta \\ -\sin\theta & \cos\theta \end{pmatrix} &= 0 \\ \begin{pmatrix} -\sin\theta\left(\frac{\partial\theta}{\partial\boldsymbol{R}} + D_{01}^{(1)}\right) & \cos\theta\left(\frac{\partial\theta}{\partial\boldsymbol{R}} + D_{01}^{(1)}\right) \\ -\cos\theta\left(\frac{\partial\theta}{\partial\boldsymbol{R}} + D_{01}^{(1)}\right) & -\sin\theta\left(\frac{\partial\theta}{\partial\boldsymbol{R}} + D_{01}^{(1)}\right) \end{pmatrix} &= 0 \end{aligned} \tag{3.1.32}$$

hence we must have

$$\frac{\partial\theta}{\partial\boldsymbol{R}} = -D_{01}^{(1)} \tag{3.1.33}$$

$$\frac{\partial\theta}{\partial\boldsymbol{R}} = -\int_{\boldsymbol{r}} d\boldsymbol{r}\zeta_0^*(\boldsymbol{r};\boldsymbol{R})\frac{\partial\zeta_1(\boldsymbol{r};\boldsymbol{R})}{\partial\boldsymbol{R}} \tag{3.1.34}$$

which can be solved as a line integral

$$\theta(\boldsymbol{R}) = -\int_{\boldsymbol{R}_0}^{\boldsymbol{R}} d\boldsymbol{R}\,\langle\zeta_0|\frac{\partial}{\partial\boldsymbol{R}}|\zeta_1\rangle \tag{3.1.35}$$

[10] $A\tilde{A} = \tilde{A}A = I$

where we choose a point $\boldsymbol{R}_0$ such that $\theta(\boldsymbol{R}_0) = 0$ which implies that $A(\boldsymbol{R}_0) = I$ and thus that at $\boldsymbol{R}_0$, diabatic and adiabatic states coincide which is the case far from the surface. The diabatic interaction matrix is thus

$$W = A^\dagger V A = \begin{pmatrix} W_{00} & W_{01} \\ W_{10} & W_{11} \end{pmatrix} \tag{3.1.36}$$

$$\begin{aligned} W_{00}(\boldsymbol{R}) &= \cos^2\theta(\boldsymbol{R})V_0(\boldsymbol{R}) + \sin^2\theta(\boldsymbol{R})V_1(\boldsymbol{R}) && (3.1.37)\\ W_{11}(\boldsymbol{R}) &= \cos^2\theta(\boldsymbol{R})V_1(\boldsymbol{R}) + \sin^2\theta(\boldsymbol{R})V_0(\boldsymbol{R}) && (3.1.38)\\ W_{01,10}(\boldsymbol{R}) &= \frac{1}{2}\sin 2\theta(\boldsymbol{R})(V_0(\boldsymbol{R}) - V_1(\boldsymbol{R})) && (3.1.39) \end{aligned}$$

The adiabatic to diabatic transformation is now finished for the two state system. Transitions that involve more that two states can be calculated using this method, however, the calculation must be broken down into a set of transitions between two states, which is inefficient. The more elegant way to do such a calculation would be to derive a new unitary transformation for an N-state system. This is done for a three state system in [2], further information on the adiabatic-diabatic representation can be found in a variety of papers including [48–50].

3.1.4 Kinetics

Thermal interaction between the bulk and the adparticle causes a kinetic process to evolve, where by energy is transferred from the bulk to the adparticle causing vibrational excitations which aid in the field evaporation process. At this point we have only considered the systems Hamiltonian excluding these thermal effects which gave us the possible energy levels, vibrational and electronic, available to the adparticle. Now we wish to understand the probability of occupation of these various levels which is impacted by the phonons of the bulk.

We now consider the interaction between the adparticle and phonons in the bulk. For this we introduce a Hamiltonian, $\hat{H}_T$ and $\hat{H}'_T$ describing the thermal vibrations in the bulk and the coupling term respectively,

$$\hat{H} = \hat{H}_a + \hat{H}_T + \hat{H}'_T. \tag{3.1.40}$$

Creation and annihilation operators, $\hat{a}^\dagger_{i\nu}$ and $\hat{a}_{i\nu}$ respectively, are used here to consider the change in occupation of different vibrational and electronic levels. The annihilation operator $\hat{a}_{i\nu}$ destroys a particle of type i (neutral or ionized) in state ν of W_{ii}. Using this formulation[11] we can rewrite the Hamiltonian in terms of creation and annihilation operators.

$$\hat{H}_a = \hat{H}^0_a + \hat{H}'_a = \sum_{i,\nu} E_{i\nu}\hat{a}^\dagger_{i\nu}\hat{a}_{i\nu} + \sum_{i,j,\nu,\mu} \langle j\mu|W_{ji}|i\nu\rangle \hat{a}^\dagger_{j\mu}\hat{a}_{i\nu} \tag{3.1.41}$$

[11] Second quantization [25, §64-65]

and assuming harmonic phonons [51, §2.5],

$$\hat{H}_T = \sum_J \hbar\omega_J \hat{b}_J^\dagger \hat{b}_J, \tag{3.1.42}$$

where $\hat{b}_J$ annihilates a phonon in normal mode $\boldsymbol{u}_J$ with frequency ω_J. The coupling term,

$$\hat{H}'_T = \sum_{i,\mu,\nu,J} X_i(\mu,\nu;J)\hat{a}_{i\mu}^\dagger(\hat{b}_J^\dagger + \hat{b}_J)\hat{a}_{i\nu}, \tag{3.1.43}$$

provides the mechanism for the adparticle to make vibrational transitions from state $\nu \to \mu$ by the absorption or emission of phonons of mode J, where

$$X_i(\mu,\nu,J) = -\sqrt{\frac{\hbar}{2\rho_0\omega_J}} \int d\boldsymbol{R}\, \eta_{i\mu}^{0*}(\boldsymbol{R})\, \boldsymbol{u}_J\, \frac{\partial W_{ii}(\boldsymbol{R})}{\partial \boldsymbol{R}} \eta_{i\nu}^0(\boldsymbol{R}) \tag{3.1.44}$$

ρ_0 is the solid density, ω_J is the phonon frequency of normal mode $\boldsymbol{u}_J$ and $\eta_{i\nu}^0$ is the ν^{th} bound state wave function for the adparticle moving in the static surface potential with potential energy W_{ii}. See [51] for detailed description.

3.1.5 The master equation

The kinetic process of field evaporation can be described generally by a master equation

$$\frac{dn_{i\nu}}{dt} = \sum_\mu \left(R_i(\nu,\mu)n_{i\mu} - R_i(\mu,\nu)n_{i\nu}\right) + \sum_{\mu,j}\left(T_{ij}(\nu,\mu)n_{j\mu} - T_{ji}(\mu,\nu)n_{i\nu}\right) \tag{3.1.45}$$

where $n_{i\nu}$ is the occupation probability of a particle of type i in state ν. $R_i(\mu,\nu)$ is the probability per unit time that a particle of type i in state ν will make a transition to the state μ and $T_{ji}(\mu,\nu)$ is probability per unit time that a particle of type i in state ν will convert to a particle of type j and make a transition to the state μ.

This equation is general indeed and could be applied to many different processes provided the definition of R, T, n include contributions from all of the relevant physical phenomenon. In the case of field evaporation processes we must include contributions from the applied electric field and any thermal vibrations in the bulk[12].

[12] In modern atom probe tomography, field evaporation is mediated with the use of a laser. The laser pulse aids in the evaporation process. Thus in future work, terms relating to laser interaction will be explicitly added. Here the applied electric field is the static applied field, and we can think of the laser interaction as providing some sort of thermal excitation. Indeed, this cannot account for and more intrinsic phenomenon related to the laser such as electronic excitation. See *Photodesorption by resonant infrared laser-adsorbate coupling, A review of the theoretical approaches by P. Piercy, Z.W. Gortel and H.J. Kreuzer* [52, ch.2] for more information on laser interaction.

Phonon transition rates $R_i(\mu,\nu)$, given in the one-phonon approximation [51, p.105], are

$$\begin{aligned} R_i(\mu,\nu) &= \frac{2\pi}{\hbar}\sum_J \frac{1}{\omega_J}|X_i(\mu,\nu;J)|^2 \times \Big[n^{(ph)}(\omega_J)\delta(E_{i\mu}-E_{i\nu}-\hbar\omega_J) \\ &\quad +(n^{(ph)}(\omega_J)+1)\delta(E_{i\mu}-E_{i\nu}+\hbar\omega_J)\Big] \end{aligned} \tag{3.1.46}$$

where the phonon occupation function is given by the Bose-Einstein function,

$$n^{(ph)}(\omega) = \frac{1}{e^{\hbar\omega/k_BT}-1}. \tag{3.1.47}$$

Due to phonon transitions there exists a finite width to each vibrational level that the adparticle can exist in [51, p.96]. In such a case we do not have levels of definite energy, thus we replace the delta function of (3.0.3) with a Lorentzian as follows

$$T_{fi} = \frac{2\pi}{\hbar}\left|\int d\boldsymbol{r}\psi_f^*(\boldsymbol{r})V_{fi}(\boldsymbol{r})\psi_i(\boldsymbol{r})\right|^2 \Delta(E_f-E_i,\Gamma_i) \tag{3.1.48}$$

$$\Delta(\varepsilon,\Gamma) = \frac{1}{2\pi}\frac{\Gamma}{\varepsilon^2+\Gamma^2/4} \tag{3.1.49}$$

$$\int_{-\infty}^{\infty} d\varepsilon\,\Delta(\varepsilon,\Gamma) = 1. \tag{3.1.50}$$

where $\delta(\varepsilon)=\lim_{\Gamma\to 0}\Delta(\varepsilon,\Gamma)$. The width[13] of the ν^{th} level of W_{ii} due to phonon transitions is given by

$$\Gamma_{i\nu} = \hbar\sum_\mu R_i(\mu,\nu). \tag{3.1.51}$$

The transition terms T rewritten in our current notation for the transition from bound state $\eta^0_{i\nu}$ of W_{ii} to continuum ionic state $\eta^0_{j\mu}$ of W_{jj} is thus

$$T_{ji}(\mu,\nu) = \frac{2\pi}{\hbar}\left|\int d\boldsymbol{R}\,\eta^{0*}_{j\mu}(\boldsymbol{R})W_{ji}(\boldsymbol{R})\eta^0_{i\nu}(\boldsymbol{R})\right|^2 \Delta(E_{j\mu}-E_{i\nu},\Gamma_{i\nu}). \tag{3.1.52}$$

The transition studied here is that of ionization, whereby a neutral atom is pulled from the surface as an ion. In this case we can calculate the total rate of formation of type j from type i particles as

$$Y_{ji} = \frac{\sum_{\mu,\nu}T_{ji}(\mu,\nu)\exp(-E_{i\nu}/k_BT)}{\sum_\nu \exp(-E_{i\nu}/k_BT)} \tag{3.1.53}$$

[13]This comes directly from the uncertainty relation for energy [25, §44] [51, p.96]

$$\Gamma \approx \hbar/\tau$$

where τ is the lifetime of the level. In this case, $R_i(\nu,\mu)$ is the probabilities per unit time that the particle of type i will transition out of the level μ into the level ν. Hence, the life time is the inverse of the sum of all possible transition rates out of the level in question.

which is a sum of the probability $T_{ji}(\mu, \nu)$ that the particle j in state μ is created from particle i in state ν weighted by the probability that particles i occupies state ν, via the Boltzmann-factor. In the case of ionization of neutral $0 \rightarrow 1+$ than $i = 0$ and $j = 1+$.

For total rate of formation Y_j of particles of type j we would sum over i. In the language of ionization, if we consider the rate of production of $2+$ ions we would consider both direct transitions and post ionization, $0 \rightarrow 2+$ and $0 \rightarrow 1+ \rightarrow 2+$ respectively.

3.2 Implementation

3.2.1 The ground state adiabatic potential energy V_0

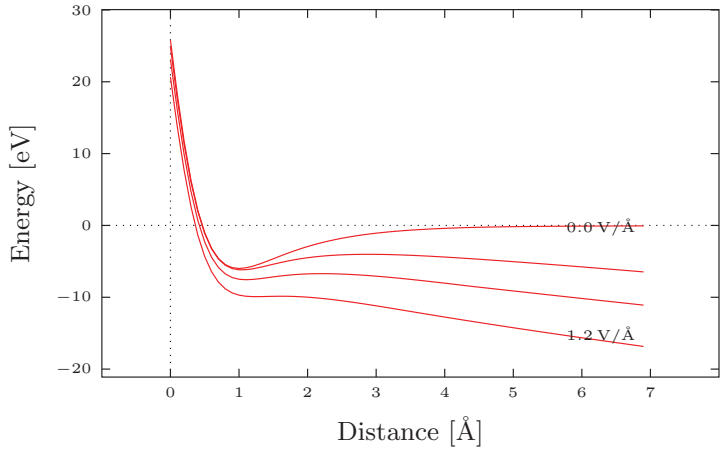

Figure 3.2: Adiabatic potential energy curves, V_0, for the field evaporation of the terminal CF_3 group leaving the remaining perfluoro-decanethiolate polymer adsorbed on Cu, applied fields of (0.0, 0.8, 1.0, 1.2) V/Å.

The adiabatic potential energy V_0 describes the evolution of the field evaporation process. The species (neutral) sits at its equilibrium distance in the potential well until given enough energy to jump over the potential energy barrier ionizing along the way. V_0 is found using DFT by calculating the energy of the system as the adparticle is moved away from the remaining structure. The electronic structure of the system is recalculated for each step the adparticle makes along the reaction path in an applied electric field. In the region of the bulk the adparticle is neutrally charged, and far from the bulk is a positively charged ion.

The polymer of interest here is perfluoro-decanethiolate given by $CF_3(CF_2)_7(CH_2)_2S-$. Evaporation was first observed experimentally with the removal of CF_3^+ at 1 V/Å, this was also seen in the ground state DFT calculations shown in earlier sections. Applying this kinetic theory we can study the rate of field evaporation for this ion. The adiabatic potential energy curves V_0 for a variety of applied electric fields were calculated for the removal of CF_3 from the remaining polymer, seen in Figure 3.2, where the distance is between the carbon of the evaporating CF_3 and the plane normal to the reaction path, intersecting the terminal carbon

of the remaining chain.

To proceed with the formalism presented above we must also calculate the first electronically excited adiabatic state V_1 and make use of the numeric solutions to wave functions of the constructed diabatic states. Instead, to simplify the numerics W_{00} and W_{11} are found by fitting a Morse potential and linear potential respectively to V_0, seen in Figure 3.3. In doing so the wave functions of both diabatic potentials are known analytically. The transition of

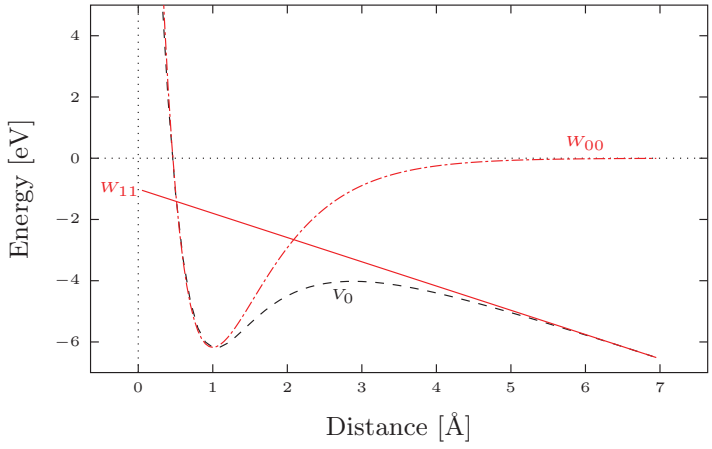

Figure 3.3: Diabatic potential energy functions W_{00} and W_{11} found through fitting the adiabatic curve V_0 of Figure 3.2 at 0.8 V/Å.

interest for field evaporation is then from a given bound state of W_{00} to a free state of W_{11}.

3.2.2 The potential energy of a neutral species W_{00}

For a neutral species to evaporate from a surface in an applied field it must overcome its own potential energy barrier given by W_{00}. The species remains neutral before, during and after field evaporation from this potential. On first glance, we would expect the depth of the potential well seen by a neutral species in an applied field to become even deeper with increasing applied field. This is because it becomes less likely for a neutral atom to evaporate, as an ion would be favoured with increasing field strength. This is indeed a general trend, however, under specific circumstances the reverse is true! A discussion of this will be given in later pages, however, the expected trends are seen in Figure 3.4.

W_{00} is approximated as a Morse potential [25, p.73] [51, p.41,115],

$$W_{00}(z) = A(e^{-2\gamma(z-z_0)} - 2e^{-\gamma(z-z_0)}) \tag{3.2.1}$$

where the bound state wave functions ψ_n, normalized in position space $\int_{-\infty}^{\infty} dz\, \psi_n^* \psi_m = \delta_{nm}$,

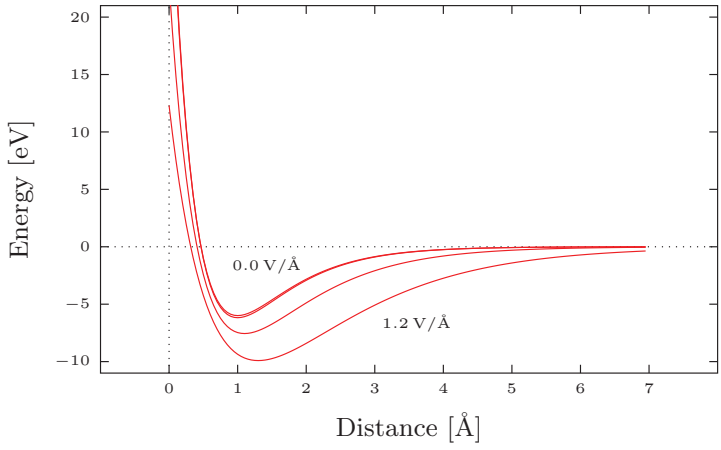

Figure 3.4: Morse fit to the region $\{0 \leq z \leq z_0 \,|\, E \leq 0\}$ of the potential energy curve for the field evaporation of the terminal CF_3 group leaving the remaining perfluoro-decanethiolate polymer adsorbed on Cu, applied fields of (0.0, 0.8, 1.0, 1.2) V/Å. Note the curve for 0.8 V/Å lay nearly atop that of 0.0 V/Å.

are given analytically in terms of Generalized Laguerre polynomials[14] L_n^α

$$\psi_n(z) = \sqrt{\gamma} f_n(\xi - \xi_0), \tag{3.2.2}$$

$$f_n(\xi) = \sqrt{\frac{n!(2\sigma_0 - 2n - 1)}{\Gamma(2\sigma_0 - n)}} (2\sigma_0 e^{-\xi})^{\sigma_0 - n - 1/2} e^{-\sigma_0 e^{-\xi}} L_n^{2\sigma_0 - 2n - 1}(2\sigma_0 e^{-\xi}) \tag{3.2.3}$$

$$\sigma_0^2 = \frac{2mA}{\hbar^2 \gamma^2} \tag{3.2.4}$$

with energies

$$E_n = -\frac{\hbar^2 \gamma^2}{2m} (\sigma_0 - n - 1/2)^2 \tag{3.2.5}$$

[14] Laguerre polynomials are in general defined in terms of confluent hypergeometric function of the first kind [53, p.509]

$$\begin{aligned} L_n^\alpha &= \frac{(\alpha+1)_n}{n!} M(-n, \alpha+1, x) \\ &= \frac{\Gamma(n+\alpha+1)}{\Gamma(\alpha+1)n!} M(-n, \alpha+1, x). \end{aligned}$$

The explicit expression is given by [53, p.775],

$$L_n^\alpha = \sum_{m=0}^{n} (-1)^m \frac{(n+\alpha)!}{(n-m)!(\alpha+m)!m!} x^m, \quad \alpha > -1$$

which we can extend for non-integer α by introducing the gamma function which states for positive integer n, $\Gamma(n+1) = n!$, hence

$$L_n^\alpha = \sum_{m=0}^{n} (-1)^m \frac{\Gamma(n+\alpha+1)}{(n-m)!\Gamma(\alpha+m+1)m!} x^m, \quad \alpha > -1.$$

where $\{n = 0, 1, 2, \ldots, N_{max} |\ N_{max} < \sigma_0 - 1/2\}$, $\xi = \gamma z$, $\xi_0 = \gamma z_0$, z_0 is the position of the minimum of the potential well, A is the depth of the well and m is the adparticles mass.

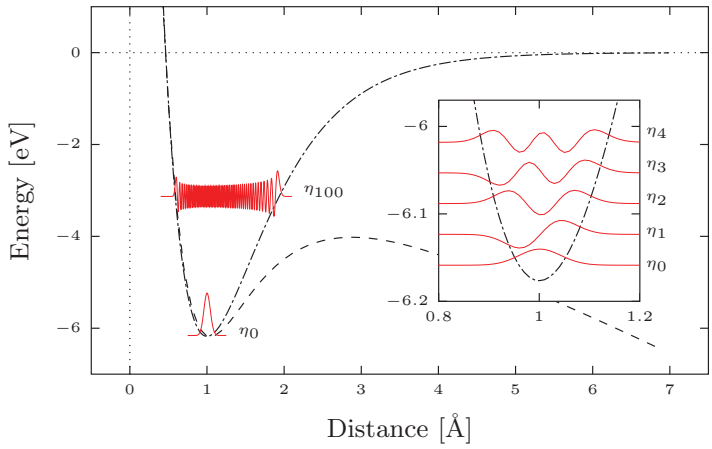

Figure 3.5: Bound state wave functions of W_{00}, fit to the region $\{0 \leq z \leq z_0 \,|\, E \leq 0\}$ of V_0, for the field evaporation of the terminal CF_3 group leaving the remaining perfluoro-decanethiolate polymer adsorbed on Cu at $0.8\,\mathrm{V/Å}$. The insert shows the wave functions for the first five levels. The adiabatic potential energy V_0 is shown as a dashed line, and W_{00} as dash-dot line.

To fit the calculated adiabatic potential energy, V_0, with a Morse potential we consider only the section from $z = 0$ to $z = z_0$. Doing a minimum search of V_0, z_0 and A are found, then in the region $0 \leq z \leq z_0$ the error is minimized between V_0 and the Morse potential to find γ. For a single atom adsorbed on a surface, the location $z = 0$ represents the surface plane and $z = z_0$ the equilibrium distance. It is not essential to fit the Morse potential to this entire range, in fact because we only wish to describe bound states we can simply fit the range $\{0 \leq z \leq z_0 | E < 0\}$. The Morse potential fit to the adiabatic potential energy for the field evaporation of the terminal CF_3 group, leaving the remaining perfluoro-decanethiolate polymer at $0.8\,\mathrm{V/Å}$, along with the bound state wave functions are shown in Figure 3.5.

3.2.3 The potential energy of ionic species W_{nn}, $n > 0$

The potential energy curve for a singly charged ion W_{11} and all diabatic potential energies for ions of higher charge[15] are given by the solution to a charged particle in a homogeneous electric field $\tilde{E}$ [25, p.74][47, p.45ff.]

$$W_{nn}(z) = -F_n z + c \tag{3.2.6}$$

$$F_n = ne\tilde{E} \tag{3.2.7}$$

[15] $W_{22}, W_{33}, \ldots$

where F_n is the electric force on the ion of charge $q = ne$. The wave functions ψ_n, normalized such that $\int_{-\infty}^{\infty} dz\, \psi_n^* \psi_m = \delta(E_n - E_m)$, are given in terms of Airy functions Φ

$$\psi_n(z) = \frac{(2m)^{1/3}}{\pi^{1/2} F_n^{1/6} \hbar^{2/3}} \Phi(-\xi) \tag{3.2.8}$$

$$\Phi(\xi) = \frac{1}{\sqrt{\pi}} \int_0^{\infty} \cos\left(\frac{1}{3}u^3 + u\xi\right) du \tag{3.2.9}$$

$$\xi = (z + (E - c)/F_n)(2mF_n/\hbar^2)^{1/2} \tag{3.2.10}$$

where m is the mass of the ion and E is its potential energy[16]. This is fit to the asymptotic slope of the adiabatic potential energy V_0. The charge of the evaporated ion is found by inverting F_n where the electric field, an input for the calculation of V_0, is known[17]. Continuing with the same data series as before, the linear potential fit for CF_3 and ionic wave function are given in Figure 3.6.

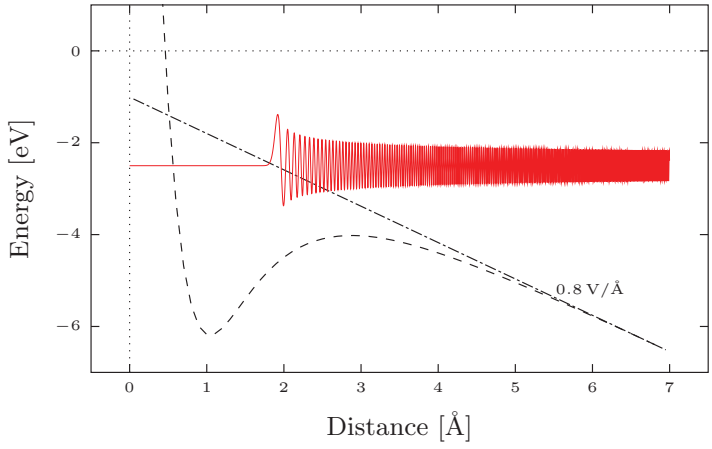

Figure 3.6: Continuum wave function with energy $-2.5\,\text{eV}$ of the potential energy W_{11}, fit to the asymptotic slope of V_0, for a singly charged CF_3 group leaving the remaining perfluorodecanethiolate polymer adsorbed on Cu with an applied field of $0.8\,\text{V/Å}$. The adiabatic potential energy V_0 is shown as a dashed line, and W_{11} as dash-dot line.

In the case, for example, where the evaporated species has a charge 2+, then the asymptotic slope will yield W_{22}. W_{11} can still be found by letting $F_1 = e\tilde{E}$, and fitting for c, this can be seen in Figure 3.7.

The kinetic energy of the field evaporated ion is of interest when dealing with time of flight spectrum. With the wave function of the field evaporated ion known the kinetic energy is easily found, $T_{ion} = -\hbar^2\nabla^2\psi/2m \propto \nabla^2\Phi(-\xi)$. Taking the second derivative in terms of z

[16]Not to be confused with the applied electric field $\tilde{E}$.

[17]The asymptotic slope should give a charge within 10% of an integer value, otherwise the calculation of V_0 is either (1) suffering from some numerical issues or (2) V_0 needs to be calculated at larger distances.

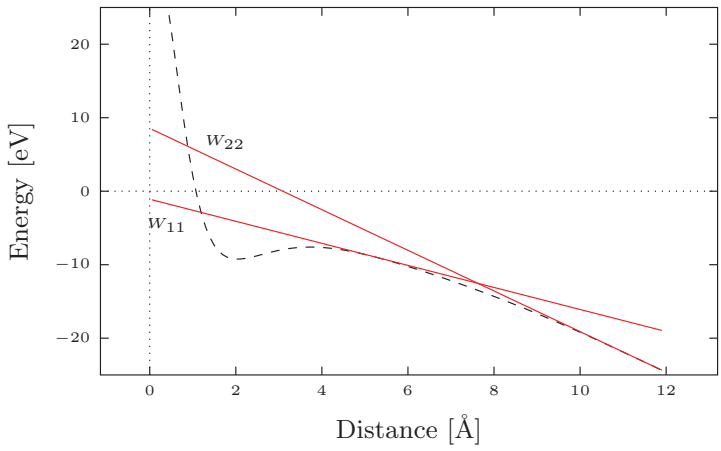

Figure 3.7: Linear fit for both W_{11} where $F_1 = e\tilde{E}$, and W_{22} given by the asymptotic slope.

we have

$$T_{ion} \quad \propto \quad z\Phi(-\xi). \tag{3.2.11}$$

At the point of field evaporation the neutral atom sitting in W_{00} is excited to a point on the potential energy curve given by W_{nn}, hence $z = (c - E)/F_n$ giving $\xi = 0$. Therefore, at the point of field evaporation the escaping ion starts with zero kinetic energy, $\Phi(0) = 0$, and gains kinetic energy with time due to the acceleration by the applied electric field.

3.2.4 Diabatic transition potential energy W_{01}, transformation angle θ, first excited adiabatic state V_1

Once V_0 is calculated and both W_{00} and W_{11} are given through fitting all other requirements can be found through simple algebraic manipulation. From the elements of (3.1.36) we can solve for,

$$\cos^2(\theta) \quad = \quad \frac{W_{11}(z) - V_0(z)}{W_{00}(z) + W_{11}(z) - 2V_0(z)} \tag{3.2.12}$$

$$V_1(z) \quad = \quad W_{00}(z) + W_{11}(z) - V_0(z) \tag{3.2.13}$$

$$W_{10} \quad = \quad -[(W_{00} - V_0)(W_{11} - V_0)]^{1/2}. \tag{3.2.14}$$

By definition in the limit of small distances ($z \to 0$) $V_0 = W_{00}$, and in the limit of large distances ($z \to \infty$) $V_0 = W_{11}$. W_{10} must therefore be only non zero in an intermediate region. Spurious values at the edges of W_{10} may be present if: (1) the DFT calculation of V_0 does not have sufficient discretization; (2) the fitting procedure of W_{00} and W_{11} is not precise enough; or (3) if the transition W_{10} is considered in the case of field evaporation of a larger ion charge such as in Figure 3.7; these values must be set to zero. An example of the form of W_{10} is given in Figure 3.8.

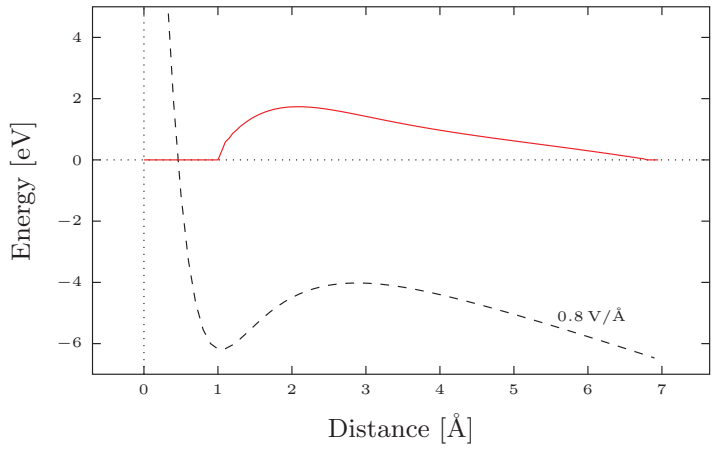

Figure 3.8: Diabatic transition potential energy W_{10} for the field evaporation of terminal CF_3 group leaving the remaining perfluoro-decanethiolate polymer adsorbed on Cu with an applied field of $0.8\,\mathrm{V/Å}$. V_0 shown as dashed line.

3.2.5 Wave function normalization

It has been mentioned in an earlier footnote that Fermi's golden rule (3.0.3) can only be interpreted as a transition rate if the initial and final wave functions are normalized in position

$$\int_{-\infty}^{\infty} d\boldsymbol{r}\psi^*\psi = 1. \tag{3.2.15}$$

This should be clear as the units of (3.0.3) would not be $[s]^{-1}$ if this were not the case. Because of this, all following formula assumed the wave functions to have this normalization.

In the case of the continuum ionic wave functions it is clear that this normalization condition can not be applied because the ionic wave functions are only bound on one side leading to a divergence in the integral. To deal with this normalization problem Z. W. Gortel, H. J. Kreuzer and R. Teshima in [54] see also [51, p.115ff.], normalize continuum wave functions of the Morse potential by imposing

$$\int_{-L}^{L} d\boldsymbol{r}\psi^*\psi = 1, \tag{3.2.16}$$

i.e. they normalize in a box of size $2L$. This effectively places a hard boundary on the right side. As they have noted this normalization cannot be done analytically. This box normalization procedure is the typical method used in textbooks and the literature when dealing with continuum wave functions.

Here, we wish to calculate a transition from a bound state in a Morse potential to a continuum state of the linear potential. This again leads to the question of how to properly normalize the un-bound wave functions. If we impose a hard boundary a similar box normalization can be carried out as done by Gortel. The potential energy curve seen by the ion

in this case would look like Figure 3.9.

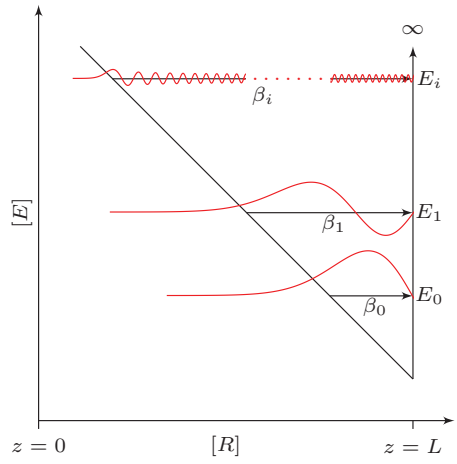

Figure 3.9: Wave functions of a triangular potential energy well given by Airy functions. β_i are the locations of the zeros of the Airy function which define the allowed states. As the width of the well L gets larger, the allowed energy levels sink to lower energies while becoming more closely spaced.

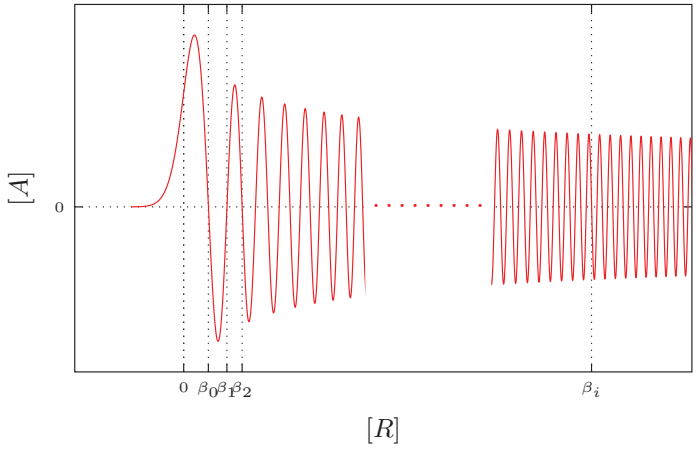

Figure 3.10: Airy function representing the wave function of a particle in homogeneous external field. β_i are the locations of the zeros. The units of amplitude $[A]$ depend on normalization.

Imposing the infinite boundary destroys the continuum resulting in discrete energy levels. For small L these energy levels are obvious as their separation is large. As the box and thus L gets larger the spacing of allowed energy levels gets smaller and smaller, tending towards a continuum. The general solution to the linear potential are Airy functions Figure 3.10, $\psi(z) = A\Phi(-\xi)$, which become highly oscillatory for large z. The allowed wave functions must vanish in the region to the right of the hard boundary. In principle this involves finding all of the zeros, β_i, of the Airy function. Then the allowed wave functions are Airy functions such that β_i resides at the position of the hard boundary, hence the enumeration i of the

zeros of the Airy function also numbers the allowed energy levels. Finding the zeros of the Airy function must be done numerically, then each bound wave function must be normalized separately by numerical integration of this highly oscillatory function. Clearly, this is not a desirable method if one is looking at more than a few states.

In general this method is required for small L as the presence of discrete states is important. However, its implementation for large L is more than computationally problematic and simply unnecessary.

A common normalization of unbound wave functions is

$$\int_{-\infty}^{\infty} d\boldsymbol{r}\phi^*_{E'}\phi_E = \delta(E' - E). \tag{3.2.17}$$

Such a normalization condition can be imposed on the continuum wave functions of the linear potential analytically, as done by Landau [25, §24]. Using wave functions with different normalization conditions leads to a problem in (3.0.3) as noted above.

In the case where the initial bound state ψ_i is normalized via (3.2.15) and final continuum state ϕ_f normalized via (3.2.17) the units of (3.0.3) would include energy[18], $[\mathrm{J}\cdot\mathrm{s}]^{-1}$. To solve this problem we simply integrate over all of the possible input energies

$$T_i = \int dE' \frac{2\pi}{\hbar} \left| \int_{-L}^{L} d\boldsymbol{r}\phi^*_f(\boldsymbol{r}; E_i + E')V_{fi}(\boldsymbol{r}; E_i)\psi_i(\boldsymbol{r}) \right|^2 \Delta(E', \Gamma_i) \tag{3.2.18}$$

where the choice of E' determines the possible final energies $E_f = E_i + E'$ of the free ionic states the particle can transition into.

We can justify this integration over energy with more than just a units argument. Consider the transition rate between an initial bound state ψ_i of a Morse potential and a group of final bound states ψ_f of the linear potential with a hard boundary enforced at L. All wave functions are thus normalized via (3.2.16). The total rate is then a sum of transitions between the discrete levels.

$$T_i = \sum_t \sum_f \frac{2\pi}{\hbar} \left| \int_{-L}^{L} d\boldsymbol{r}\psi^*_f(\boldsymbol{r})V_{fi}(\boldsymbol{r})\psi_i(\boldsymbol{r}) \right|^2 \delta(E_f - E_i - E_t) \tag{3.2.19}$$

where E_t is some externally supplied energy to make the transition. If only a single energy E_t is supplied, than only a single term in the double sum will survive due to conservation of energy seen in the term $\delta(E_f - E_i - E_t)$. The sum can be written as an integral provided there is a dense set of final levels E_f and transition energies E_t such that transitions to a group of densely spaced final levels is considered. Introducing dummy variables E and E'

$$T_i = \int dE'\, g_t(E') \int dE\, g_f(E)\, \frac{2\pi}{\hbar} \left| \int_{-L}^{L} d\boldsymbol{r}\psi^*_f(\boldsymbol{r})V_{fi}(\boldsymbol{r})\psi_i(\boldsymbol{r}) \right|^2 \delta(E - E_i - E'), \tag{3.2.20}$$

[18] A delta function has units inverse to the argument. In this case it should be clear that ϕ normalized by (3.2.17) has units $[J \cdot r]^{-1/2}$.

where $g_f(E)$ is the density of final states given for discrete states as

$$g_f(E) = \sum_f \delta(E - E_f) \tag{3.2.21}$$

and where the number of states between E_1 and E_2 is given by integrated density of states

$$G_f(E) = \int_{E_1}^{E_2} dE\, g_f(E), \tag{3.2.22}$$

and similarly $g_t(E)$ is the density of states for allowed transition energies.

Due to the normalization the allowed ionic wave functions are not only a function of position but defined for a given energy and normalization distance hence, $\psi_f(\boldsymbol{r}) = \psi_f(\boldsymbol{r}; E_f, L)$. Similarly the density of allowed states in the ionic potential depends on the normalization condition $g_f(E) = g_f(E; L)$. As L increases the amplitude of ψ_f decreases for a given energy as the absolute square integral must always equal unity (3.2.16). Also with increasing L the integrated density of states $G_f(E; L)$ for any given energy range $E \pm \varepsilon$ increases without bound as the spacing of allowed levels decreases for a given energy.

Consider now the limit

$$\lim_{L\to\infty} g_f(E; L)\, \frac{2\pi}{\hbar} \left| \int_{-L}^{L} d\boldsymbol{r} \psi_f^*(\boldsymbol{r}; E, L) V_{fi}(\boldsymbol{r}) \psi_i(\boldsymbol{r}; E_i) \right|^2 \delta(E - E_i - E'). \tag{3.2.23}$$

Defining a new final state wave function

$$\phi_f^*(\boldsymbol{r}; E, L) = \sqrt{g_f(E; L)}\ \psi_f^*(\boldsymbol{r}; E, L) \tag{3.2.24}$$

we have

$$\begin{aligned}
&\lim_{L\to\infty} \int_{-L}^{L} d\boldsymbol{r}\, \phi_f^*(\boldsymbol{r}; E', L) \phi_f(\boldsymbol{r}; E, L) \\
&\qquad = \lim_{L\to\infty} \int_{-L}^{L} d\boldsymbol{r}\, \sqrt{g(E'; L)}\ \psi_f^*(\boldsymbol{r}; E', L) \sqrt{g(E; L)}\ \psi_f(\boldsymbol{r}; E, L) \\
&\qquad = \lim_{L\to\infty} \sqrt{g(E'; L) g(E; L)} \int_{-L}^{L} d\boldsymbol{r}\, \psi_f^*(\boldsymbol{r}; E', L) \psi_f(\boldsymbol{r}; E, L) \\
&\qquad = \begin{cases} \infty & E = E' \\ 0 & E \neq E' \end{cases} \\
&\qquad = \delta(E' - E).
\end{aligned} \tag{3.2.25}$$

Hence, the transition rate from a single bound state ψ_i normalized via $\int_{-\infty}^{\infty} d\boldsymbol{r} \psi^* \psi = 1$ to a

range of continuum unbound states ϕ_f normalized via $\int_{-\infty}^{\infty} d\boldsymbol{r}\phi^*_{E'}\phi_E = \delta(E'-E)$ is given by,

$$\begin{aligned} T_i &= \int dE'\, g_t(E') \int dE\, \frac{2\pi}{\hbar} \left| \int_{-\infty}^{\infty} d\boldsymbol{r}\phi_f^*(\boldsymbol{r};E) V_{fi}(\boldsymbol{r}) \psi_i(\boldsymbol{r};E_i) \right|^2 \delta(E - E_i - E') \\ &= \int dE'\, g_t(E') \frac{2\pi}{\hbar} \left| \int_{-\infty}^{\infty} d\boldsymbol{r}\phi_f^*(\boldsymbol{r};E_i+E') V_{fi}(\boldsymbol{r}) \psi_i(\boldsymbol{r};E_i) \right|^2 \end{aligned} \tag{3.2.26}$$

where the bounds of energy integration for energy E' define the range of transition energies allowed and hence the range in final energy states you wish to attempt a transition into. If only a single transition energy is supplied, i.e. $g_t(E') = \delta(E'-E_0)$, this does not represent an exact transition between two levels but rather a transition between the bound state ψ_i and a band of continuum states $\{\phi_f\}$ of width dE in energy around $E_i + E_0$. Checking the units of (3.2.26), we see $dE' \to [\mathrm{J}]$, $g_t \to [\mathrm{J}]^{-1}$, $\hbar \to [\mathrm{J}\cdot\mathrm{s}]$, $\phi \to [\mathrm{J}\cdot\mathrm{r}]^{-1/2}$, $V_{fi} \to [\mathrm{J}]$, $\psi \to [\mathrm{r}]^{-1/2}$, giving the units of $T \to [\mathrm{s}]^{-1}$ as expected [19].

The above can be extended to the ion yield equation (3.1.53) giving

$$Y = \frac{\sum_i T_i \, \exp(-E_i/k_BT)}{\sum_i \exp(-E_i/k_BT)}. \tag{3.2.27}$$

The density of states $g_t(E)$ for transition energies can alternatively be thought of as spread of the initial bound state level, due to phonons for example. Using earlier notation for transitions of type i particles in state ν of the Morse potential to type j particles in state μ of the linear potential.

$$Y_{ji} = \frac{\sum_\nu \int dE_\mu \, t_{ji}(\mu,\nu) \exp(-E_{i\nu}/k_BT)}{\sum_\nu \exp(-E_{i\nu}/k_BT)} \tag{3.2.28}$$

where

$$t_{ji}(\mu,\nu) = \frac{2\pi}{\hbar} \left| \int d\boldsymbol{R}\, \eta^{0*}_{j\mu}(\boldsymbol{R};E_\mu) W_{ji}(\boldsymbol{R}) \eta^0_{i\nu}(\boldsymbol{R};E_\nu) \right|^2 \Delta(E_\mu - E_\nu, \Gamma_{i\nu}) \tag{3.2.29}$$

and it is understood that the normalization of the bound states of the Morse potential is given by (3.2.15) and continuum states of the linear potential is given by (3.2.17). The spread of the initial bound state level is given by the Lorentzian $\Delta(E_\mu - E_\nu, \Gamma_{i\nu})$ where $\Gamma_{i\nu}$ is the width.

3.2.6 Width of bound state levels and occupation

If we consider a potential well with discrete levels then the density of states will be a sum of delta functions centred at the allowed energies. This gives an integrated density of states that looks like a stair case, increasing in steepness as the spacing between levels deceases, as shown in Figure 3.11.

[19] This mixing of normalization conditions is hinted at in [25, §43] and carried out, albeit for a different case and condition than is presented here, in [25, §90].

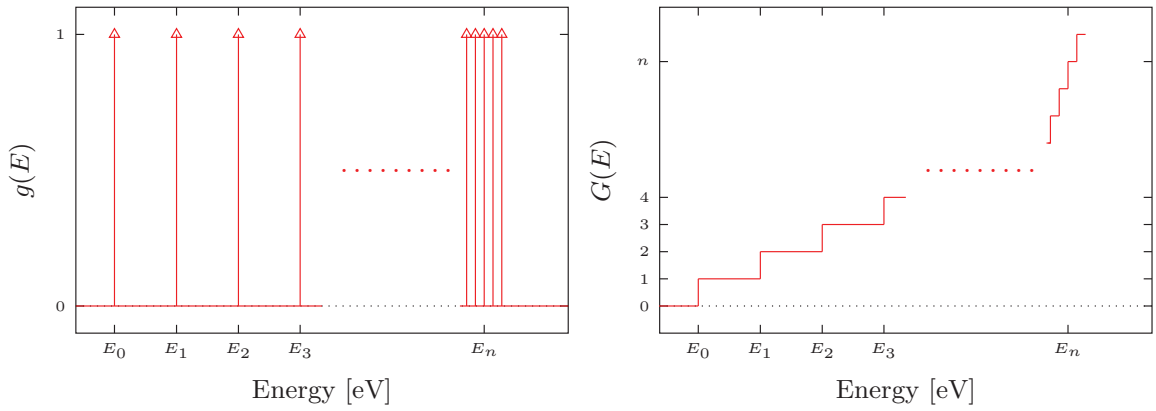

Figure 3.11: Left: Density of states (left), $g(E)$; Right: integrated density of states, $G(E)$, for discrete bound states. Each level contributes a delta function to the density of states, where the spacing between allowed levels becomes smaller as energy increases.

Due to the finite lifetime of a given bound energy level there is a natural width given by Heisenberg's uncertainty principle, $\Delta E \approx \frac{\hbar}{\Delta t}$, meaning that energy levels are only considered discrete if the width is much less than the spacing between levels, $\Delta E = \Gamma << E_m - E_n$. These new broadened levels are expressed as a Lorentzian, seen in Figure 3.12, making the density of states a smooth function of energy

$$g(E) = \sum_n \frac{1}{2\pi} \frac{\Gamma}{(E - E_n)^2 + \Gamma^2/4} \tag{3.2.30}$$

given in Figure 3.13.

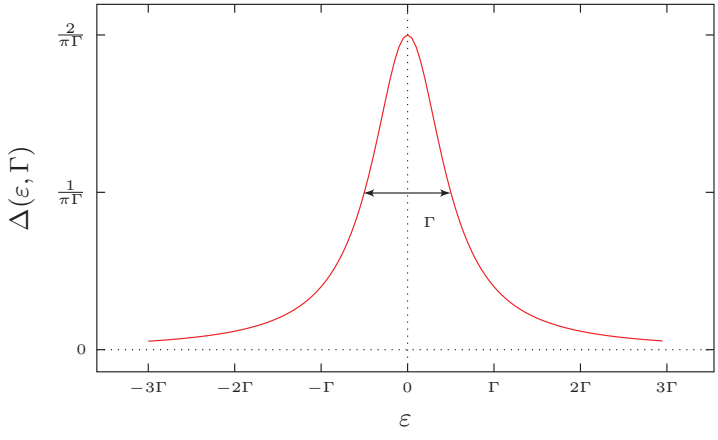

Figure 3.12: Lorentzian profile for the extent of a bound state energy level. This is the density of states as a function of energy.

To calculate the level width, (3.1.51), we require a complete knowledge of the material of interest, i.e. the field evaporation tip in this case. The purpose of the atom probe is to measure this structure exactly, thus the three dimensional structure is not known a priori.

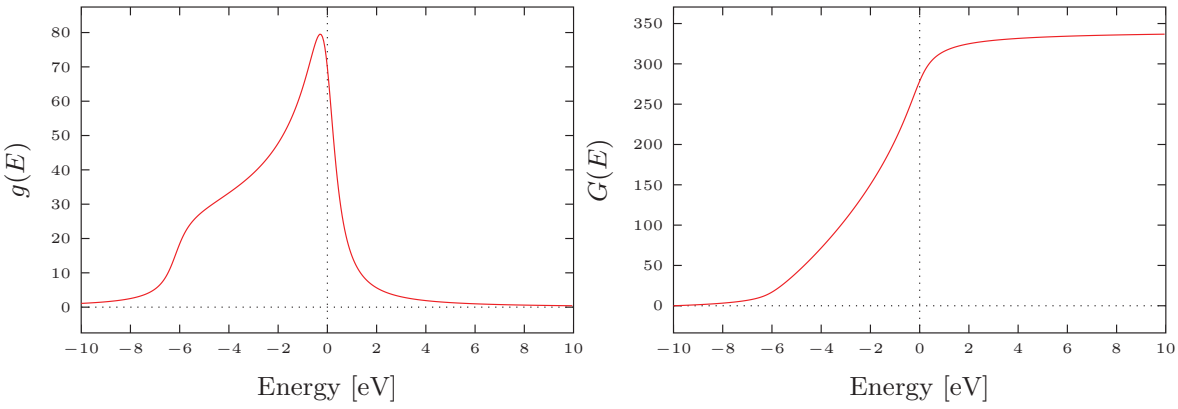

Figure 3.13: Left: Density of states, $g(E)$; Right: integrated density of states, $G(E) = \int_{-\infty}^{E} dE' g(E')$, for the bound states of CF_3 at 0.8 V/Å, where each level contributes a Lorentzian with a width of 1 eV.

Assuming a theoretical crystal structure allows for the calculation to be carried out as done in [2] for bulk phonon modes for helium on tungsten, xenon on tungsten is also covered in [51][55]. For larger molecules, the bound-bound transition rates required to know the level width Γ have not been calculated exactly. A value of 1eV is taken as a constant across all calculations. This source of error can be corrected with careful calculation, as will be done in future work. For now, the parameter Γ is a source of question, however, its impact is predictable and does not change the trends in ion yield, only the order of magnitude shown here[20].

3.3 Field evaporation of polymers

Starting with the species predicted by our ground state DFT calculations, CF_3, the adiabatic potential energy curves V_0 for a variety of applied electric fields were calculated. These curves have been shown earlier for the single copper atom base model, Figure 3.2. The phenomenon of electrostriction is evident when looking at the depth of the minimum of these curves. For this we can also look at the depth of the diabatic potential energy curves for the neutral species, W_{00}, given by the Morse potential energy fit. As noted earlier we would expect that with increasing applied field the depth of W_{00} would increase as it becomes less likely for a neutral species to field evaporate. In the case of perfluoro-decanethiolate it was shown in earlier DFT calculations that due to the electronegativity of the fluorine groups the polymer first compresses in fields below 0.6 V/Å. This compression increases the force of repulsion

[20]The transition rates for exact initial and final levels will be in error as the allowed final states are strongly dependent on Γ. Here, we are interested in the ion yield which involves an integration over the individual bound state transitions. Hence this effect does not carry through, changing Γ results in a simple shift in the graph of yield verses temperature. Note this argument only holds where the level width's dependence on temperature is weak. This is only true at low temperature. The level width becomes more dependent on temperature as it increases which can change the ion yield trend.

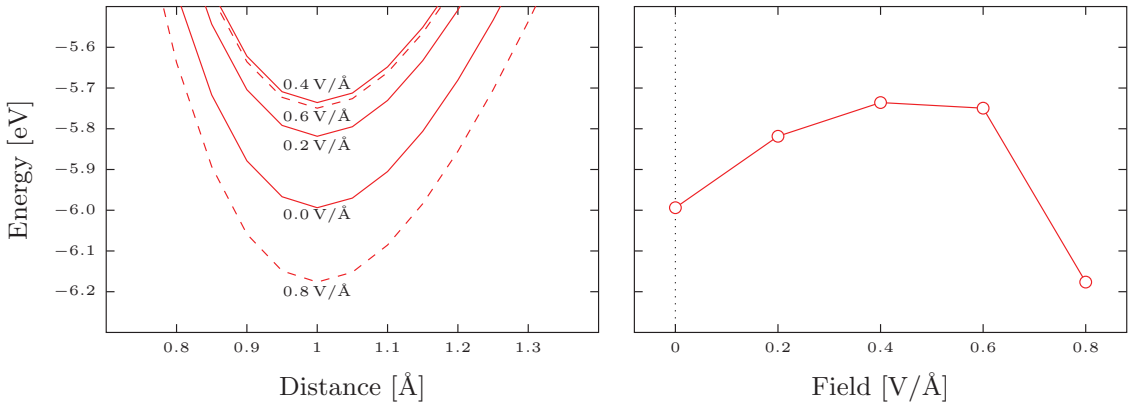

Figure 3.14: Left: W_{00} in the region of the minimum for the field evaporation of the terminal CF_3 group leaving the remaining perfluoro-decanethiolate polymer adsorbed on Cu, applied fields of (0.0, 0.2, 0.4, 0.6, 0.8) V/Å. Right: The minimum of W_{00} as a function of applied field.

between atoms thus the overall potential energy of the system is larger. We can see from Figure 3.14 that the depth of W_{00} decreases until 0.6 V/Å where it begins to increase again, this turning point is where compression of the polymer stops and stretching begins. The increase in potential energy due to compression makes it more likely for neutral species to field evaporate. This trend is solely due to the compression in low applied fields.

When a neutral particle is ionized it makes a transition from a position in W_{00} to W_{11}. If we consider the ground state transition as shown in Figure 3.15 the particle sits in the minimum of W_{00}. Bound tightly by its walls it vibrates back and forth in a small region shown by its wave function. In this ionization process the maximum transition rate from the ground state is to a final potential energy state directly above the peak in the ground state wave function. A plot of the ground state wave function of W_{00} and the wave function of W_{11} for which this maximum transition rate occurs are shown in Figure 3.15, along with a plot of the transition rate as a function of final potential energy for the field evaporation of the terminal CF_3 from perfluoro-decanethiolate on Cu at 0.8 V/Å. The created ion has zero kinetic energy at this point which was shown earlier. The ion is however accelerated by the applied electric field, thus gains kinetic energy with time.

It should be clear from (3.2.29) that the maximum transition rate occurs when the product of the bound and ionic wave functions with W_{10} is largest. Because of this product, transitions to regions where one of these three functions is zero are zero. Transition rates from higher levels in W_{00} show a similar form to that of the ground state, however change in magnitude and become further modulated by the oscillatory nature of the wave functions of the higher bound states.

To calculate the time of flight spectrum the position of the detector must be known. When ionization occurs, the position of the ion in space is determined by the final energy state in W_{11} to which the transition is made. The starting point of the ion in space is therefore at

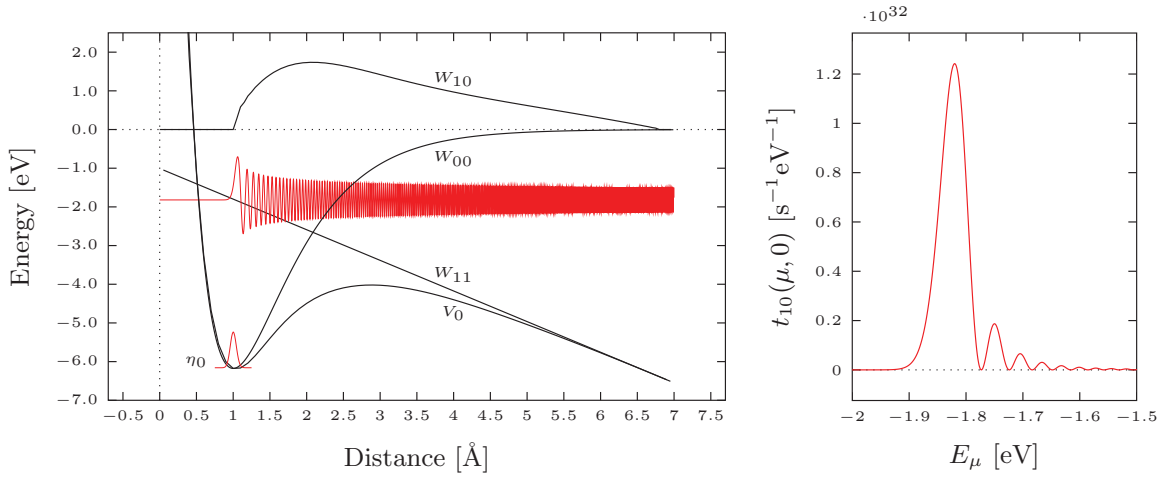

Figure 3.15: Right: Transition rate $t_{10}(\mu, 0)$ from the ground state of W_{00} to a final energy state μ of W_{11} for the field evaporation of the terminal CF_3 from perfluoro-decanethiolate on Cu at 0.8 V/Å. The maximum transition rate from the ground state is to a final energy state in W_{11} of -1.82 eV. Left: Wave functions and potentials involved in this transition rate from the ground state.

some point along the line W_{11}. Because the starting kinetic energy of the ions is zero the spread in the measured time of flight spectrum is determined by the range in final potential energy states of W_{11} for which a transition is made. As an example if the position of the particle when ionization occurs is $z = c - E_\mu/F$, the time of flight is then given by $t = \sqrt{2D/a}$ where $D = d - z$ is the distance the ion must travel to hit the detector at d and $a = F/m$ is the acceleration of the ion by the applied electric field. Equivalently, one can simply plot the ion yield as a function of the final potential energy state in W_{11}.

In this case, the transition rate $t_{10}(\mu, 0)$ from the ground state of W_{00} as a function of final potential energy E_μ in W_{11}, shown in Figure 3.15, is visually identical to the ion yield as a function of E_μ at temperatures in the region of 50 K and below as only the ground state is significantly occupied. Looking at (3.2.28), if only the ground state is occupied than the exponential terms drop out leaving

$$Y_{10} = \int dE_\mu \, t_{10}(\mu, 0) \tag{3.3.1}$$

hence the total ion yield here is simply the integral of the curve shown in Figure 3.15.

A surface map for the transition rate $t_{10}(\mu, \nu)$ plotted beside the maximum transition rate for each bound level ν of W_{00} is shown in Figure 3.16 for the same CF_3 model. The maximum transition rate occurs between the initial and final states corresponding to the energy for which $W_{00} = W_{11}$ which in this case is -2.7 eV as seen in Figure 3.16. Transition rates from these high bound levels do not come into play at realistic temperatures as they are not occupied. In fact, with a difference in energy of $\Delta E_{10} = 0.03$ eV between the ground state and first excited state of W_{00} for this model, temperatures in the region of 350 K would

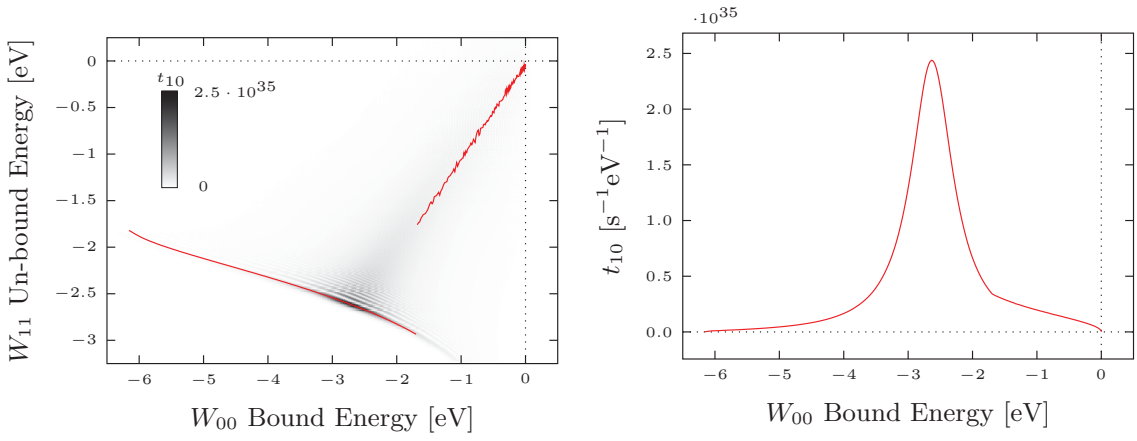

Figure 3.16: Left: Surface map for the transition rate $t_{10}(\mu, \nu)$ for the field evaporation of the terminal CF_3 group leaving the remaining perfluoro-decanethiolate polymer adsorbed on Cu at 0.8 V/Å. The maximum transition rate for each bound level ν of W_{00} is highlighted by the overlaid red line. Right: The maximum transition rate $t_{10}(\mu, \nu)$ for each bound level ν of W_{00}.

be required to allow significant occupation of the first excited vibrational state. Hence, for temperatures below this value ion yield is exclusively a result of ionization from the ground state, i.e. no temperature dependence.

Because only the ground state is significantly occupied, the ion yield is severely dependent on the Morse potential energy fit W_{00}, specifically the location of the minimum. This should be clear as the transition rate (3.2.29) depends on the product of W_{10} with the wave functions of the bound W_{00} and free ionic W_{11} respectively, where only the ground state of W_{00} is relevant. If the process of interest is thermally activated than this becomes less apparent as more of the bound levels become occupied and the ground state becomes less important. Here, the accuracy and discretization in the calculation of V_0, from which W_{00} is found, is of utmost importance. Slight shifts in the position of the minimum will not lead to a change in the trend of the final result but will change the order of magnitude.

The maximum transition rate follows the leading peak of the bound state wave function of W_{00}, i.e. the maximum transition rate will occur to a potential energy level in W_{11} directly above this peak. This makes sense as the leading peak of the bound state wave function is the largest, see for example η_{100} in Figure 3.5. At a point after, but in the region of the $W_{00} = W_{11}$ crossing, the maximum transition rate occurs between levels of the same energy. This is seen in Figure 3.16 where the maximum transition rate $t_{10}(\mu, \nu)$ is highlighted in red and there is a discontinuous jump at -1.7 eV. This line $E_\mu = E_\nu$ is a result of energy conservation, all transitions where $E_\mu \neq E_\nu$ would not occur if the bound levels of W_{00} were infinitely sharp as discussed earlier. The fluctuation seen in Figure 3.16 for the region where the maximum transition occurs for $E_\mu = E_\nu$ is a result of the calculation. Less care was taken in the calculation of this section due to its irrelevance in the process of interest.

To compare the ion yield of a variety of possible field evaporated species the same model must be used. Here field evaporation of CF_3^+, $C_2F_5^+$ and $C_3F_7^+$ will be compared, in this case all from the remaining perfluoro-decanethiolate polymer adsorbed on Cu_3 to allow a slightly larger electron sink for the larger species. Note in this case we are not looking at successively field evaporated species. Rather, we comparing the rates of possible evaporated species that are first to leave the complete chain. In other words, for the field evaporation of CF_3 the remaining chain is $(CF_2)_7(CH_2)_2S - Cu_3$ and for the field evaporation of C_2F_5 the remaing chain is $(CF_2)_6(CH_2)_2S - Cu_3$ etc.. For each species, a different V_0 in a variety of applied electric fields must be calculated, and for each of these curves the corresponding diabatic potentials are constructed.

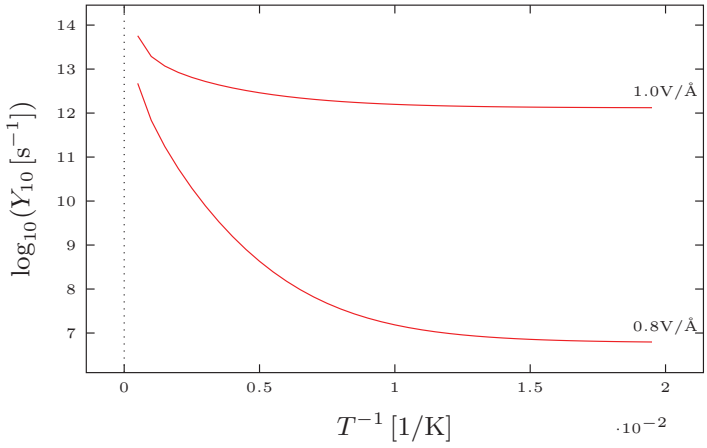

Figure 3.17: Ion yield for the field evaporation of the terminal CF_3 group leaving the remaining perfluoro-decanethiolate polymer adsorbed on Cu_3 enforcing $F = q\tilde{E},\ q = 1.0e$.

Plotted in Figure 3.17 is the ion yield as a function of inverse temperature for the field evaporation of CF_3 at 0.8 V/Å and 1.0 V/Å. The temperature ranges from 50 K − 2000 K, lower temperatures are not plotted as the yield is constant. The ion yield in the experimentally valid low temperature region is a constant as only the ground state of W_{00} is occupied. As the temperature increases there begins to be thermal excitation which leads to the occupation of higher energy levels in the bound state and thus easier field evaporation. As a result, the ion yield is larger for higher temperatures. It is also clear from this graph that there is a significant difference in the ion yield for different applied electric fields especially in the temperature region around 50 K, in this case being five orders of magnitude difference between 0.8 V/Å and 1.0 V/Å.

The peak temperature of the atom probe tip in the experiment was estimated to be 200 K during the short laser pulses used to initiate field evaporation [1]. This temperature would allow for occupation of the first excited vibrational level in W_{00} leading to the start of dependence on temperature. An investigation into the nature of laser interaction with insulating materials [20] showed that the laser pulses provided a dominant electronic excitation and not a thermal excitation with dielectrics in atom probe experiments. In this case, the laser

pulse would not directly heat the SAM but the underlaying metal bulk. The SAM would take a longer time, on the order of picoseconds, to become thermally activated, by this point the metal bulk would have conducted the majority of heat away. This finding suggests that the SAM would remain in the region for which the yield is independent of temperature. An explicit implementation of laser interaction would be the next step in development for this theory.

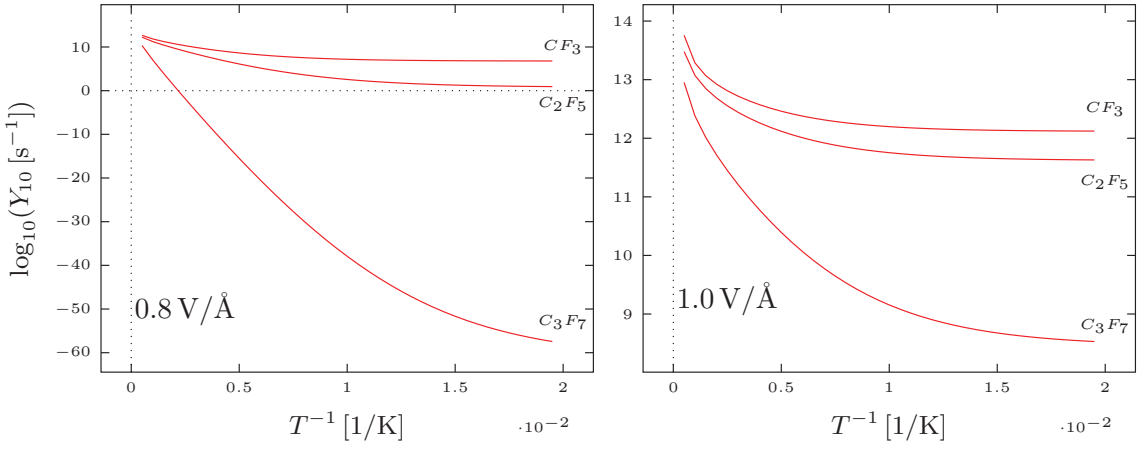

Figure 3.18: Ion yield for the field evaporation of the terminal $CF_3/C_2F_5/C_3F_7$ groups leaving the remaining perfluoro-decanethiolate polymer adsorbed on Cu_3 enforcing $F = q\tilde{E},\ q = 1.0e$ at 0.8 (left) and 1.0V/Å (right).

Moving on to the final comparison, Figure 3.18 shows the ion yield of different field evaporated species from the complete perfluoro-decanethiolate polymer. As expected it is more difficult to field evaporate a larger molecule; this is seen especially at the lower applied field of 0.8 V/Å. Interestingly, there is a large increase in yield for both $C_2F_5^+$ and $C_3F_7^+$ when the applied field is increased to 1.0 V/Å. Yield at 50 K for CF_3^+ and $C_2F_5^+$ are within an order of magnitude which should be the case as both of these species are seen experimentally in this applied field region [1]. In the same scenario, the yield of $C_3F_7^+$ is three order of magnitude smaller, and was not reported in the experiment.

3.4 Summary

The Kinetic theory of field evaporation first developed for metals by Kreuzer et al. [2] was applied to the field evaporation of perfluoro-decanethiolate. The field evaporation of this polymer was shown to not be a thermally activated process in the experimental temperature region around 50 K. Ionization occurs directly from the ground state of the diabatic potential W_{00} as a result of electron tunnelling from the evaporated species to the bulk. At the point of ionization the ion has zero kinetic energy and is accelerated away from the bulk by the applied electric field. The interesting phenomenon of electrostriction was also reflected in the

depth of the Morse potential energy curves W_{00} fit to the calculation of the adiabatic energy curves V_0 for the field evaporation of CF_3.

Unlike the ground state density functional calculations of field evaporation this theory allowed for a comparison between possible field evaporation species. The comparison given here was between CF_3^+, $C_2F_5^+$ and $C_3F_7^+$. The most probable field evaporated species was CF_3, agreeing with the DFT calculations of previous sections. The yield of the second most probable species C_2F_5 was within an order of magnitude of CF_3 which agrees with the experiment to the extent that these two species are seen evaporating in the same field region. Finally, the yield of C_3F_7 fell three orders of magnitude behind.

It is this comparison between species that makes this theory appealing in conjunction with the usual ground state density functional calculations. The most probable species given by the earlier DFT calculations was confirmed by this theory. Furthermore, this kinetic theory gives us a comparison between the rate of field evaporation of other species, which cannot be had from the earlier calculations. This provides us with an understanding not only of the most likely species but other less probable but in some cases still significant species.

4. Conclusion

Perfluoro-decanethiolate as a single polymer was studied using time independent density functional theory. The first point of interest is the possible field evaporated species. These species are given experimentally with the use of mass spectrum data, and hence theoretical calculations of such species provides an initial check of the model. The simple model of a single polymer chosen here showed agreement with initial field evaporation namely CF_3/C_2F_4, however began to deviate in the later stages of field evaporation. Larger species seen in experiment such as SC_9F_4 where not seen in this model and thus may be a result of bulk interaction not included here.

The HOMO/LUMO gap was shown to decrease with increasing applied electric field, agreeing with current research on insulating and semiconducting materials in high electric fields. Other interesting trends such as electrostriction and precursors to field evaporation such as changing dipole moment were also studied. In the case of electrostriction, perfluoro-decanethiolate was compressed in low applied fields before stretching leading up to field evaporation. This trend was closely linked to that of the dipole moment, which was initially negative but was reversed at higher applied fields due to the induced charge separation.

This single polymer model is in no way exhaustive, however it provides a necessary starting point for further investigation. The angle an individual polymer in a monolayer makes with the underlaying metal surface is still an area of interest when an electric field on the order of volts per angstrom is applied. Geometrical changes to the monolayer prior to field evaporation would indeed have an effect on atom probe experiments, specifically sample reconstruction. The model presented here is clearly lacking in the areas of surface and neighbouring polymer interactions. Both of these interactions must be included in future studies to gain an understanding of bulk geometrical changes and shielding of the electric field. These interactions would also alter the field evaporated species seen. Calculating field evaporation from larger clusters of polymers is the next step in understanding this process. Increasing the size of the cluster, calculated in the Gaussian09 software package, vastly increases the computational effort. This effort quickly becomes unmanageable rendering Gaussian09 all but useless for such large scale calculations. Instead, the use of periodic boundary conditions (PBC) could be the next step for these calculations. It should be noted that in a PBC calculation the unit cell must be chosen large enough such that the entire surface layer is not field evaporated at once.

A significant improvement would be the introduction of time dependent density functional theory (TDDFT). Improvements in this area are currently being lead by K. Watanabe and his group at the Tokyo University of Science where their cutting edge research is introducing laser interaction from first-principles, see for example [56–58]. Laser pluses are used to initiate field evaporation in atom probe experiments, and this is a key interaction missing in the DFT

models presented here. The use of such advanced techniques will lead to a more detailed look at this small system and more realistic sized samples.

A kinetic theory of field evaporation based on Fermi's Golden rule was used to complement the initial DFT study of perfluoro-decanethiolate. This theory was shown to agree with the most probable evaporated species given by DFT, namely CF_3. Further information on alternate evaporated species was also given along with dependence on temperature. The ion yield provides a direct comparison to the rate of detection of ions in experiment, and was shown to not be a thermally activated process in the experimental temperature region. This theory not only provides new information on the field evaporation process but does so with minimal computational effort. The most costly area is the computation of the ground-state adiabatic potential-energy curves V_0, via DFT. This however, takes a fraction of the time that the DFT methods presented in the first section requires. Calculation of these V_0 curves can be done prior to any knowledge of the species seen in DFT. Once V_0 is known, the yield can be calculated. Ordering the species in terms of yield then provides the dominant evaporation sequence.

Further work must be undertaken to include all factors involved in the field evaporation process. The main point of interest aside from the use of larger DFT models in the calculation of the adiabatic potential energy curves, V_0, would be the implementation of laser interaction, as noted above. The experimental field evaporation of perfluoro-decanethiolate was initiated with the use of a pulsed laser. Although a recent study [20] suggested that the laser pulse initiates field evaporation with a dominant electronic excitation, not thermal excitation, it remains to be seen how this laser interaction affects the results of this theory. Introducing an effective change in temperature due to this laser interaction would not change the present development, however any electronic excitation must be added. An exact calculation of the width of bound state energy levels should also be carried out. This should be done specifically for the thermally activated region where the width becomes dependent on temperature.

The use of two different normalization conditions, for the wave functions of W_{00} and W_{11}, led to incredible computational savings that should be remembered when implementing this method in future transition rate calculations. Although the ion yield was shown to be a result of transitions from the ground state alone, in the experimental temperature region, future implementation of laser interaction and a larger DFT model may change this. In the case where thermal activation is relevant, there will be more than one bound level contributing to the ion yield. This normalization method will show its merit even more as the number of relevant levels increase.

This work has provided a starting point, which will most certainly lead to some interesting physics. It should be clear that DFT, although broad in its applicability, is not the only theory that can be employed to study field evaporation. The kinetic theory presented here was first developed to look a the field evaporation of metals in 1990 [2] and is for the first time here being used to look at field evaporation of polymers with intriguing results begging for a followup.

Bibliography

[1] A. Stoffers, C. Oberdorfer, and G. Schmitz. Controlled field evaporation of fluorinated self-assembled monolayers. *Langmuir*, 28(1):56–59, 2012.

[2] H.J. Kreuzer, K. Watanabe, and L.C. Wang. Theory of field desorption and field ionization: Thermal field desorption of helium. *Surface Science*, 232:379–392, 1990.

[3] B. Gault, M.P. Moody, J.M. Cairney, and S.P. Ringer. *Atom Probe Microscopy*. Number 160 in Springer Series in Materials Science. Springer, 2012.

[4] C. Oberdorfer, S.M. Eich, and G. Schmitz. A full-scale simulation approach for atom probe tomography. *Ultramicroscopy*, 128:55–67, 2013.

[5] C. Oberdorfer, S.M. Eich, M. Lütkemeyer, and G. Schmitz. Applications of a versatile modelling approach to 3D atom probe simulations. *Ultramicroscopy*, http://dx.doi.org/10.1016/j.ultramic.2015.02.008, 2015.

[6] N. Rolland, D.J. Larson, B.P. Geiser, S. Duguay, F. Vurpillot, and D. Blavette. An analytical model accounting for tip shape evolution during atom probe analysis of heterogeneous materials. *Ultramicroscopy*, http://dx.doi.org/10.1016/j.ultramic.2015.03.010, 2015.

[7] F. Vurpillot and C. Oberdorfer. Modeling atom probe tomography: A review. *Ultramicroscopy*, http://dx. doi.org/10.1016/j.ultramic.2014.12.013, 2015.

[8] H.J. Kreuzer. *Chemistry and Physics of Solid Surfaces VIII*, volume 22 of *Springer Series in Surface Sciences*, pages 133–158. Springer-Verlag, 1990.

[9] H.J. Kreuzer. Physics and chemistry in high electric fields. *Surface Science*, 246:336–347, 1991.

[10] H.J. Kreuzer. *Surface Science of Catalysis: In Situ Probes and Reaction Kinetics*, volume 482 of *ACS Symposium Series*, pages 268–286. American Chemical Society, 1992.

[11] H.J. Kreuzer, L.C. Wang, and N.D. Lang. Self-consistent calculation of atomic adsorption on metals in high electric fields. *Phys. Rev. B*, 45(20):12050–12055, 1992.

[12] Y. Suchorski, W.A. Schmidt, N. Ernest, J.H. Block, and H.J. Kreuzer. Electrostatic fields above individual atoms. *Progress in Surface Science*, 48(1-4):121–134, 1995.

[13] Y. Suchorski, N. Ernest, W.A. Schmidt, V.V. Medvedev, H.J. Kreuzer, and R.L.C. Wang. Field desorption and field evaporation of metals. *Progress in Surface Science*, 53(2-4):135–153, 1996.

[14] J.D. Jackson. *Classical Electrodynamics*. Wiley, 3 edition, 1998.

[15] B. Mazumder, A. Vella, B. Deconihout, and Tala'at Al-Kassab. Evaporation mechanisms of MgO in laser assisted atom probe tomography. *Ultramicroscopy*, 111:571–575, 2011.

[16] M. Karahka and H.J. Kreuzer. Field evaporation of oxides: A theoretical study. *Ultramicroscopy*, 132:54–59, 2013.

[17] E.P. Silaeva, M. Karahka, and H.J. Kreuzer. Atom probe tomography and field evaporation of insulators and semiconductors: Theoretical issues. *Curr. Opin. Solid State Mater. Sci.*, 17(5):211–216, 2013.

[18] M. Karahka and H.J. Kreuzer. Field evaporation of insulators and semiconductors: Theoretical insights for ZnO. *Ultramicroscopy*, http://dx.doi.org/10.1016/j.ultramic.2015.03.011i, 2015.

[19] Y. Xia, M. Karahka, and H.J. Kreuzer. Field evaporation of ZnO: A first-principles study. *J. Appl. Phys.*, 118:025901, 2015.

[20] E.P. Silaeva, L. Arnoldi, M.L. Karahka, B. Deconihout, A. Menand, H.J. Kreuzer, and A. Vella. Do dielectric nanostructures turn metallic in high-electric dc fields? *Nano Lett.*, 14:6066–6072, 2014.

[21] O. Nishikawa and M. Taniguchi. Atom-by-atom analysis of non-metallic materials by the scanning atom probe. *Chinese Journal of Physics*, 43(1-II):111–123, 2005.

[22] L.R.C. Wang, H.J. Kreuzer, and O. Nishikawa. Polythiophene in strong electrostatic fields. *Organic Electronics*, 7:99–106, 2006.

[23] B. Gault, W. Yang, K. Ratinac, R. Zheng, F. Braet, and S. Ringer. Atom probe microscopy of self-assembled monolayers: Preliminary results. *Langmuir*, 26(8):5291–5294, 2010.

[24] Y. Zhang and A. Hillier. Three-dimensional atom probe tomography of oxide, anion, and alkanethiolate coatings on gold. *Anal. Chem.*, 82:6139–6147, 2010.

[25] L. Landau and E. Lifshitz. *Quantum mechanics, Non-relativistic Theory*, volume 3 of *Course of Theoretical Physics*. Butterworth Heinemann, 3 edition, 2003.

[26] A. Szabo and N.S. Ostlund. *Modern Quantum Chemistry: Introduction to Advanced Electronic Structure Theory*. Dover Publications, 1996.

[27] R. Parr and W. Yang. *Density functional theory of atoms and molecules*. Oxford University Press, 1989.

[28] M. Levy. Universal variational functionals of electron densities, first-order density matrices, and natural spin-orbitals and solution of the v-representability problem. *Proc. Natl. Acad. Sci. USA*, 76(12):6062–6065, 1979.

[29] A. Groß. *Theoretical Surface Science*. Springer-Verlag, 2009.

[30] N.W. Ashcroft and N.D. Mermin. *Solid State Physics*. Harcourt College Publishers, 1976.

[31] W. Kohn and L. Sham. Self-consistant equations including exchange and correlation effects. *Physical Review*, 140(4A):1133–1138, 1965.

[32] A.D. Becke. A new mixing of hartree–fock and local density functional theories. *J. Chem. Phys.*, 98(2):1372–1377, 1993.

[33] A.D. Becke. Density functional thermochemistry. iii: The role of exact exchange. *J. Chem. Phys.*, 98(7):5648–5652, 1993.

[34] P.J. Stephens, F.J. Devlin, C.F. Chabalowski, and M.J. Frisch. Ab initio calculation of vibrational absorption and circular dichroism spectra using density functional force fields. *Physical Chemistry*, 98(45):11623–11627, 1994.

[35] F. Jensen. *Computational Chemistry*. Wiley, 2 edition, 2007.

[36] J. Lowe and K. Peterson. *Quantum Chemistry*. Elsevier, 3 edition, 2006.

[37] C. Cramer. *Essentials of Computational Chemistry*. Wiley, 2 edition, 2004.

[38] M.J. Frisch, G.W. Trucks, H.B. Schlegel, G.E. Scuseria, M.A. Robb, J.R. Cheeseman, G. Scalmani, V. Barone, B. Mennucci, G.A. Petersson, H. Nakatsuji, M. Caricato, X. Li, H.P. Hratchian, A.F. Izmaylov, J. Bloino, G. Zheng, J.L. Sonnenberg, M. Hada, M. Ehara, K. Toyota, R. Fukuda, J. Hasegawa, M. Ishida, T. Nakajima, Y. Honda, O. Kitao, H. Nakai, T. Vreven, J.A. Montgomery, Jr., J.E. Peralta, F. Ogliaro, M. Bearpark, J.J. Heyd, E. Brothers, K.N. Kudin, V.N. Staroverov, R. Kobayashi, J. Normand, K. Raghavachari, A. Rendell, J.C. Burant, S.S. Iyengar, J. Tomasi, M. Cossi, N. Rega, J.M. Millam, M. Klene, J.E. Knox, J.B. Cross, V. Bakken, C. Adamo, J. Jaramillo, R. Gomperts, R.E. Stratmann, O. Yazyev, A.J. Austin, R. Cammi, C. Pomelli, J.W. Ochterski, R.L. Martin, K. Morokuma, V.G. Zakrzewski, G.A. Voth, P. Salvador, J.J. Dannenberg, S. Dapprich, A.D. Daniels, Ö. Farkas, J.B. Foresman, J.V. Ortiz, J. Cioslowski, and D.J. Fox. Gaussian09 revision d.01. Gaussian Inc. Wallingford CT 2009.

[39] K. Riley, M. Hobson, and S. Bence. *Mathematical methods for physics and engineering*. Cambridge, 3 edition, 2006.

[40] R.L.C. Wang, H.J. Kreuzer, M. Grunze, and A.J. Pertsin. The effect of electrostatic fields on an oligo(ethylene glycol) molecule : dipole moments, polarizabilities and field dissociation. *Phys. Chem. Chem. Phys.*, 2(1721-1727), 2000.

[41] H.J. Kreuzer. *Nonequilibrium Thermodynamics and its Statistical Foundations*. Oxford University Press, 1981.

[42] E.H. Hauge and J.A. Stovneng. Tunneling times: a critical review. *Rev. Mod. Phys.*, 61(4):917–936, 1989.

[43] A.S. Landsman and U. Keller. Tunnelling time in strong field ionisation. *J. Phys. B: At. Mol. Opt. Phys.*, 47(204024), 2014.

[44] A.S. Landsman, M. Weger, J. Maurer, R. Boge, A. Ludwig, S. Heuser, C. Cirelli, L. Gallmann, and U. Keller. Ultrafast resolution of tunneling delay time. *Optica*, 1(5):343–349, 2014.

[45] A.S. Landsman and U. Keller. Attosecond science and the tunnelling time problem. *Physics Reports*, 547:1–24, 2015.

[46] M. Buttiker and R. Landauer. Traversal time for tunneling. *Phys. Rev. Lett.*, 49(23):1739–1742, 1982.

[47] D.A.B. Miller. *Quantum Mechanics, for Scientists and Engineers*. Cambridge University Press, 2008.

[48] M. Baer. Adiabatic and diabatic representations for atom-molecule collisions: Treatment

of the collinear arrangement. *Chem. Phys. Lett.*, 35(1):112–118, 1975.

[49] C.A. Mead and D.G. Truhlar. Conditions for the definition of a strictly diabatic electronic basis for molecular systems. *J. Chem. Phys.*, 77(12):6090–6098, 1982.

[50] M. Baer and R. Englman. A study of the diabatic electronic representation within the Born-Oppenheimer approximation. *Mol. Phys.*, 75(2):293–303, 1992.

[51] H.J. Kreuzer and Z.W. Gorte. *Physisorption Kinetics*, volume 1 of *Springer Series in Surface Sciences*. Springer-Verlag, 1986.

[52] S.H. Lin, editor. *Advances in Multi-Photon Processes and Spectroscopy*, volume 3. World Scientific, 1987.

[53] M. Abramowitz and I.A. Stegun. *Handbook of Mathematical Functions: with Formulas, Graphs, and Mathematical Tables*. National Bureau of Standards, corrected edition 10 edition, 1972.

[54] Z.W. Gortel, H.J. Kreuzer, and R. Teshima. Desorption by phonon cascades for gas-solid systems with many physisorbed surface bound states. *Phys. Rev. B*, 22(12):5655–5670, 1980.

[55] Z.W. Gortel, H.J. Kreuzer, R. Teshima, and L.A. Turski. Kinetic equations for desorption. *Phys. Rev. B*, 24(8):4456–4469, 1981.

[56] D. Utsugi, C. Hu, and K. Watanabe. Laser-driven field emission from graphene nanoribbons: Time-dependent density-functional theory simulations. *Appl. Phys. Express*, 5:105101, 2012.

[57] J. Haruyama, C. Hu, and K. Watanabe. First-principles molecular-dynamics simulation of biphenyl under strong laser pulses by time-dependent density-functional theory. *Phys. Rev. A*, 85:062511, 2012.

[58] T. Higuchi, C. Hu, and K. Watanabe. Energetics and dynamics of laser-assisted field emission from silicene nanoribbons: Time-dependent first-principles study. *e-J. Surf. Sci. Nanotech.*, 13:115–120, 2015.